

www.acsnano.org

Targeted Intracellular Delivery of Trastuzumab Using Designer Phage Lambda Nanoparticles Alters Cellular Programs in **Human Breast Cancer Cells**

Alexis Catala, Monika Dzieciatkowska, Guankui Wang, Arthur Gutierrez-Hartmann, Dmitri Simberg, Kirk C. Hansen, Angelo D'Alessandro, and Carlos E. Catalano*



Downloaded via UNIV COLORADO ANSCHUTZ MEDICAL CMPS on June 20, 2022 at 15:10:34 (UTC) See https://pubs.acs.org/sharingguidelines for options on how to legitimately share published articles.

Cite This: ACS Nano 2021, 15, 11789-11805



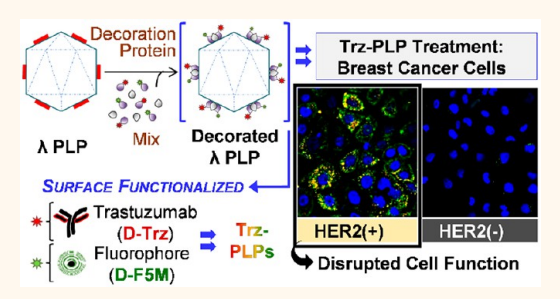
ACCESS

Metrics & More

Article Recommendations

Supporting Information

ABSTRACT: | Several diseases exhibit a high degree of heterogeneity and diverse reprogramming of cellular pathways. To address this complexity, additional strategies and technologies must be developed to define their scope and variability with the goal of improving current treatments. Nanomedicines derived from viruses are modular systems that can be easily adapted for combinatorial approaches, including imaging, biomarker targeting, and intracellular delivery of therapeutics. Here, we describe a "designer nanoparticle" system that can be rapidly engineered in a tunable and defined manner. Phage-like particles (PLPs) derived from bacteriophage lambda possess physiochemical properties compatible with



pharmaceutical standards, and in vitro particle tracking and cell targeting are accomplished by simultaneous display of fluorescein-5-maleimide (F5M) and trastuzumab (Trz), respectively (Trz-PLPs). Trz-PLPs bind to the oncogenically active human epidermal growth factor receptor 2 (HER2) and are internalized by breast cancer cells of the HER2 overexpression subtype, but not by those lacking the HER2 amplification. Compared to treatment with Trz, robust internalization of Trz-PLPs results in higher intracellular concentrations of Trz, prolonged inhibition of cell growth, and modulated regulation of cellular programs associated with HER2 signaling, proliferation, metabolism, and protein synthesis. Given the implications to cancer pathogenesis and that dysregulated signaling and metabolism can lead to drug resistance and cancer cell survival, the present study identifies metabolic and proteomic liabilities that could be exploited by the PLP platform to enhance therapeutic efficacy. The lambda PLP system is robust and rapidly modifiable, which offers a platform that can be easily "tuned" for broad utility and tailored functionality.

KEYWORDS: viral nanotechnology, biomedical engineering, precision medicine, breast cancer, HER2 signaling, metabolic reprogramming, omics technologies

iruses are protein complexes that naturally assemble into nanoparticles via a caged architecture (capsid) that is optimized for intracellular delivery of protein and nucleic acid cargo to specific targets in biological systems. 1-3 From a bionanomaterial standpoint, the innate propensity to form soluble, monodisperse structures with defined but tunable symmetry makes viruses highly attractive platforms that can be repurposed for the targeted delivery of diagnostic and therapeutic (theranostic) payloads.⁴⁻⁶ However, the success of viral nanoparticles (VNPs) derived from eukaryotic viruses (e.g., retroviridae, adenoviridae) has been tempered by safety concerns related to pathogenicity, immunogenicity, and toxicity.^{7,8} In this regard, platforms developed using bacteriophages (phages) offer distinct

advantages, 9,10 such as being noninfectious to mammalian cells¹¹ and biocompatible in vivo (animal models, ^{12,13} humans 14,15) and having the capacity to be economically prepared in large-scale industrial processes.¹⁶

Phages have historically been used as model organisms to study basic molecular mechanisms of genetic regulation and virus assembly. 2,17 Additionally, they form the foundation of

Received: April 5, 2021 Accepted: June 17, 2021 Published: June 30, 2021





common research technologies (e.g., gene expression systems, phage display)^{2,4} and have been employed as therapeutic agents (e.g., phage therapy^{15,18}). Diverse genetic and chemical approaches have been implemented in adapting phage systems for nanoscale engineering of phage-like particles (PLPs).^{7,10} The PLP capsid functions as a prefabricated nanoscaffold whose exterior can be modified to display large and small molecules. For example, PLPs derived from phages P22, lambda, T4, AP205, and MS2 have been used to display foreign proteins and peptides such as (i) transmembrane signaling cytokine CD154 and peptides derived from CD154 and CD47;⁵ (ii) transferrin,¹⁹ GFP,²⁰ and peptides derived from aspartate β -hydroxylase²¹ and human epidermal growth factor receptor 2 (HER2);^{22,23} (iii) β -galactosidase and Y. pestis antigens;¹² (iv) E. coli maltose binding protein, P. falciparum antigens and peptides derived from mutant sequences of human telomerase reverse transcriptase and human epidermal growth factor receptor 1 (HER1);²⁴ and (v) aptamers against Jurkat leukemia T-cells. 25 Additionally, filamentous phage systems (e.g., M13, fd) have been simultaneously modified with polymer chains, imaging groups, and antibody fragments to HER1 and HER2.²⁶ In all cases, PLP surface functionalization was accomplished by genetic or chemical modification of proteins that form or are associated with the capsid structure (capsid proteins, decoration proteins, nonessential outer capsid proteins). Further, the PLP interior can be used to encapsulate and protect sensitive payloads such as enzymes (e.g., alcohol dehydrogenase by P22,27 superoxide dismutase by $Q\beta^{28}$), small molecules (e.g., imaging agents and organic compounds by P22^{29,30}), and nucleic acids (e.g., DNA molecules by T4¹² and lambda, ²⁰ functional RNAs by $Q\beta^{31}$ and $\varphi 29^{32}$).

Our lab has developed a "designer" lambda PLP platform.³³ When coexpressed in E. coli, the lambda major capsid protein (gpE) and scaffolding protein (gpNu3) self-assemble into spherical PLPs (~50 nm).³⁴ These precursor shells (Naked PLPs) are then artificially expanded in vitro to yield icosahedral shells (~60 nm) composed of 420 copies of gpE, which resemble the expanded capsid of the infectious phage during DNA packaging.³⁵ Naked PLPs are stabilized by the addition of the decoration protein (gpD), which assembles as trimeric spikes at the 3-fold axes of the icosahedron (140 trimers, 420 copies);^{36,37} particles decorated entirely with wild-type gpD are referred to as WT PLPs. Notably, N- and C-terminal fusion constructs of gpD have been utilized with great success in lambda phage display applications, 4,38 and heterologous genetic fusion constructs can also be used in our platform to decorate the shell exterior in vitro.20 Further, we have engineered a gpD variant to contain a sole cysteine residue (gpD(S42C)) that can be chemically modified with nonproteinaceous molecules (e.g., polyethylene glycol, mannose) and subsequently used to decorate PLPs. 20 Lambda PLPs can thus be decorated with modified gpD proteins, alone or in combination, to display various molecules (biological, synthetic) in defined surface ratios.^{20,33}

In the present study, we describe a potential theranostic platform of lambda PLPs that simultaneously display an imaging probe (fluorescein-5-maleimide, F5M) and a biologic (trastuzumab, Trz), which are referred to as Trz-PLPs. F5M was incorporated due to its biocompatibility and use as a common model of anionic fluorophores, ³⁹ whereas Trz enables targeting of cancer cells with the *HER2* amplification. ⁴⁰ Of note, Trz (Herceptin; Genentech; South San Francisco, CA,

USA) was designed to selectively target the extracellular domain (domain IV)41 of HER2 (also known as CD340 and ErbB2, Erb-B2 receptor tyrosine kinase 2), which is frequently overexpressed in breast, gastric, and esophageal cancers 42 and correlates with a poor clinical prognosis. 40,43 This biologic became the standard first-line treatment for HER2-positive (HER2+) metastatic breast cancer after seminal studies by Slamon⁴⁴ and others^{40,45} demonstrated that Trz administered alone or in combination with chemotherapeutic drugs results in significant tumor regression and enhanced patient survival. 46 Despite the substantial achievements of HER2-targeted therapies, challenges in cancer treatment remain, including systemic toxicity and intrinsic and acquired resistance to current therapeutics. 43,47 This necessitates fundamental investigations to develop additional technologies for sole and/or combination therapies in this setting.

As a proof of concept, we first show that purified PLP preparations possess physiochemical properties that comply with pharmaceutical standards. We then characterize the biological consequences of HER2 receptor binding relative to free Trz (native gold-standard) using breast carcinoma cell lines. We demonstrate that robust internalization of Trz-PLPs by HER2⁺ cells results in higher intracellular concentrations of the modified biologic and affects several cellular programs, including altering the metabolic and proteomic landscapes of HER2⁺ cells. These studies inform the rational design of the lambda PLP system and confirm that this platform can be utilized to elicit changes in biological function that could benefit cancer therapy.

RESULTS AND DISCUSSION

Engineering Fluorescent, HER2-Targeting PLPs. The development of multifunctional nanoparticles is not only of technological interest, nanoparticle platforms also have the potential of addressing key shortcomings of current therapies (e.g., systemic toxicity, onset of multidrug resistance). As,49 Virus-based nanomaterials present diverse candidates for the development and improvement of nanomedicines,7,50 and have been widely used as vaccines and gene delivery vectors since the 1970s. The nanoparticle platform presented here demonstrates the utility of lambda-derived PLPs as a potential cancer therapeutic. The engineering of lambda PLPs using both genetic and chemical approaches is shown schematically in Figure 1A. The shell exterior can be diversely modified with biological, organic, and/or synthetic molecules in defined display densities, highlighting the versatility of the platform.

To track lambda PLPs in cell-based assays, we first constructed a fluorescent decoration protein (D-F5M) by chemical cross-linking of F5M to the sole cysteine residue in gpD(S42C), as outlined in Figure 1B-1. Stoichiometric labeling was confirmed by denaturing polyacrylamide gel electrophoresis (SDS-PAGE) (Supplementary Figure S1A, lane 3) and mass spectrometry (data not shown). To incorporate receptor specificity in the design, we next constructed a HER2targeting decoration protein (D-Trz) using Trz and a maleimide-succinimidyl valerate bifunctional cross-linker (Figure 1B-2). Size-exclusion chromatography (SEC) was used to purify Trz, gpD, D-F5M, and D-Trz, and the chromatograms are presented in Figure S1B. Whereas the synthesis of the fluorescent construct is constrained by the reactivity of a single residue (site-specific modification), D-Trz results in a heterogeneous mixture due to the chemical modification of the biologic by lysine amide coupling. Considering that Trz

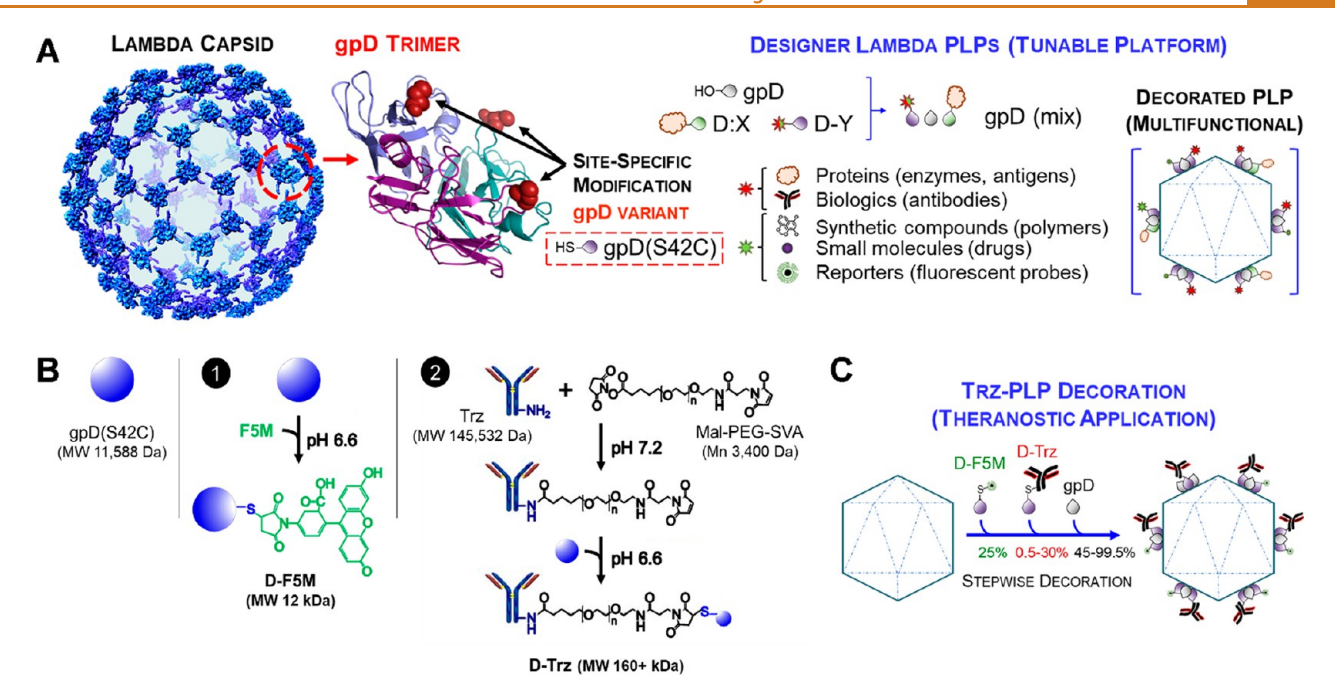


Figure 1. Lambda phage-like particle (PLP) platform. (A) Cryo-electron microscopy reconstruction of the expanded phage lambda capsid lattice, showing only the density from the decoration protein assembled as trimeric spikes at the quasi 3-fold axes (420 copies of gpD). Crystal structure of a single gpD trimer (PDB #1C5E) is shown to the right in cartoon representation and modified to display the serine to cysteine mutation (red spheres) of the gpD variant (gpD(S42C)). Wild-type gpD, gpD fusion constructs (D:X), and chemically modified gpD(S42C) constructs (D-Y) can be used, alone or in combination, to decorate the shell surface of lambda PLPs in a defined manner to engineer multifunctional particles. (B) We focus on chemical modification of gpD(S42C) to generate constructs containing a reporter (fluorescein-5-maleimide, F5M) or biologic (trastuzumab, Trz), as demonstrated by the reaction schematics using (1) thiol-maleimide chemistry to yield D-F5M and (2) lysine amide coupling followed by thiol-maleimide chemistry to yield D-Trz. (C) PLPs were then simultaneously decorated with these constructs—Trz-PLPs (25% D-F5M, 0.5–30% D-Trz)—to examine the theranostic potential of the lambda PLP platform.

contains 90 lysine residues, a single antibody likely contains multiple gpD adducts. Indeed, the protein-banding pattern obtained for D-Trz reveals three distinct bands with relative molecular weights of 39, 62, and 120 kDa (Figure S1A, lane 7). This suggests that Trz modified with gpD(S42C) contains a single gpD addition on the light chain and at least two gpD additions on the heavy chain; thus, we estimate that there are an average of 3-6 decoration proteins per antibody. While the chemical modification of Trz was successful and FDAapproved antibody-drug conjugates employing the same strategy have an average drug-to-antibody ratio of 3.5-4 drug molecules per antibody, 52,53 we acknowledge the limitations of using a native IgG molecule as the targeting ligand. For instance, antibodies are large molecules (~150 kDa) that contain multidomain architectures with binding sites for proteins involved in complement activation and antibody recognition.⁵⁴ We are currently developing gpD-affibody constructs (<20 kDa) as cell-targeting moieties^{54,55} to curtail some of these pharmaceutical concerns.

Next, purified PLPs were simultaneously decorated with 25% D-F5M and 0.5–30% D-Trz to generate Trz-PLPs with various surface densities of the biologic, as outlined in Figure 1C. Surface density is denoted as a percentage based on the total number of gpD copies that are required for full occupancy of the gpD binding sites (420 total) on the shell surface. Therefore, the surface of Trz-PLPs contains approximately 105 copies of D-F5M and 2–126 copies of D-Trz per particle, with the remaining gpD binding sites filled using wild-type gpD. As controls for particle preparations, PLPs were decorated entirely with wild-type gpD (WT PLPs) or 25% D-F5M (F5M-PLPs;

remaining gpD binding sites occupied by wild-type gpD). Decorated PLPs were purified by SEC (Figure S1C,D) and stored at 4°C until use. No changes to particle composition or functionality were observed after 4 months of storage. Of note, the lambda PLP platform described here can be rapidly redesigned to include other or additional multimodality probes, biologics, and/or compounds. This includes replacing the fluorophore used with an IR dye more amenable to *in vivo* imaging ⁵⁶ and the addition of synthetic polymers to improve pharmacokinetic parameters, ⁵⁷ enzymatic inhibitors to inhibit specific protein—protein interactions, ^{47,58} and/or cytotoxic agents to enhance the therapeutic effect, ⁵⁹ as depicted in Figure 1A.

Characterization of Trz-PLPs. The physiochemical properties of PLP preparations were characterized by multiple approaches. Agarose gel electrophoresis (AGE) and SDS-PAGE analyses demonstrate that the surface densities of both gpD constructs (D-F5M, D-Trz) can be adjusted in a defined manner, and constructs remain associated with the shells after purification (Figure 2A,B). Transmission electron microscopy (TEM) reveals homogeneous particle dispersions of decorated PLPs that retain icosahedral symmetry (Figure 2C). Unlike WT PLPs, Trz-PLPs display a density that projects further from the shell surface and that matches the morphology of free Trz. We also note the formation of a protein corona in Trz-PLP preparations that becomes denser as the surface density of D-Trz is increased and results in increases of up to 16 nm in overall particle diameter (Table S1). This confirms that D-Trz can effectively be used to decorate PLPs.

ACS Nano www.acsnano.org Article

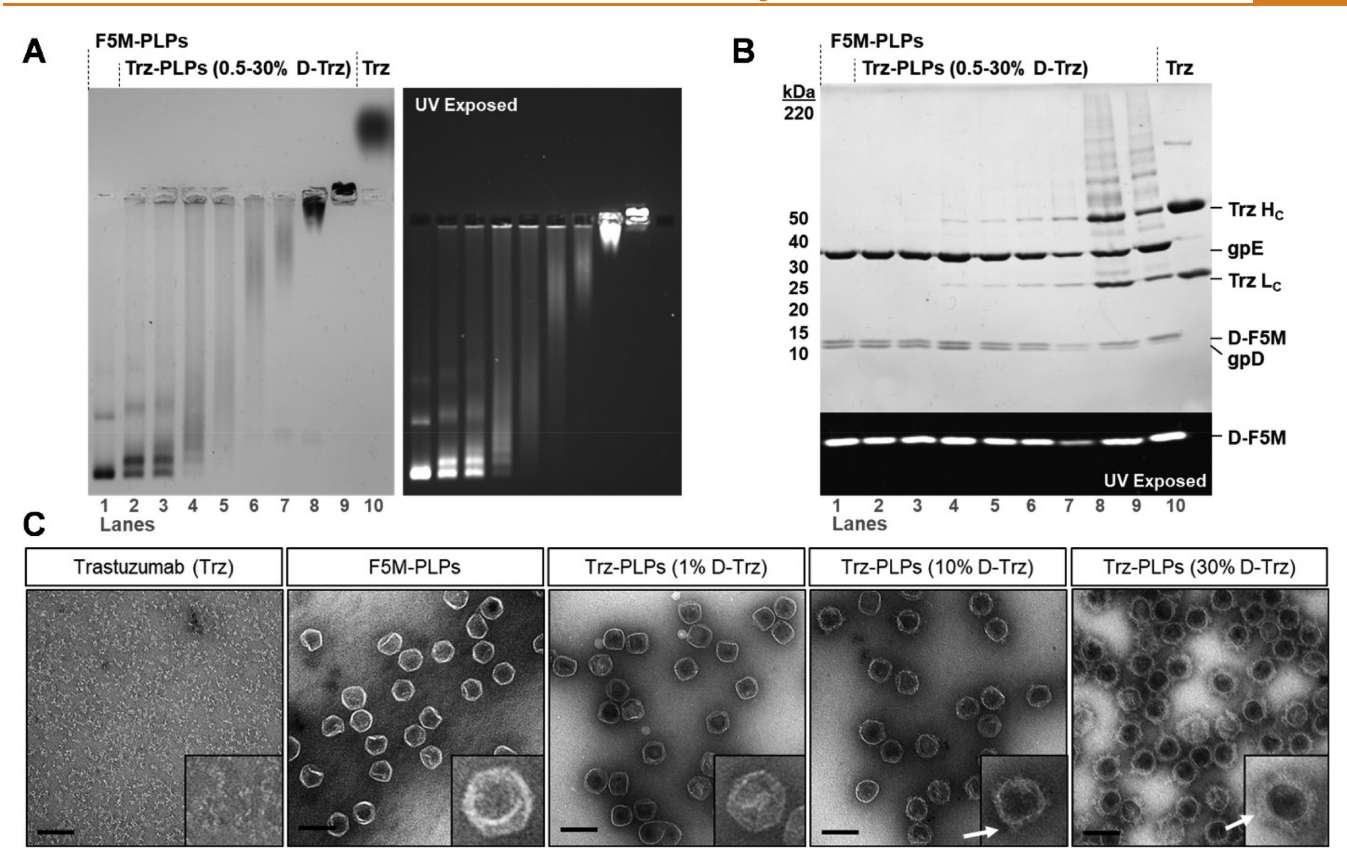


Figure 2. Characterization of decorated lambda PLPs. PLPs were decorated using mixtures of gpD proteins and purified by SEC. (A) Purified particles were fractionated by AGE and visualized by Coomassie Blue staining (left) and fluorescence (right). Lanes: (1) F5M-PLPs (25% D-F5M); (2–9) Trz-PLPs (25% D-F5M and either 0.5%, 1%, 2%, 4%, 6%, 10%, 20%, or 30% D-Trz); (10) Trz (free, native). (B) SDS-PAGE analysis of purified PLPs visualized by Coomassie Blue staining (top) and fluorescence (bottom). Lanes 1–10 were loaded in the same order as (A). The migration of Trz heavy and light chains (Trz H_C , Trz L_C), the lambda major capsid and decoration proteins (gpE, gpD), and D-F5M are indicated. (C) Electron micrographs of purified materials at 120 000× magnification (enlarged view, inset). Black scale bars represent 100 nm. White arrows indicate the density attributed to D-Trz on the surface of Trz-PLPs (visible \geq 4% D-Trz).

Changes to particle size were corroborated by dynamic light scattering (DLS) analysis, as indicated by the higher hydrodynamic size of Trz-PLPs (Table S1, Z-average (Zave), intensity size distribution (int size dist)). Additionally, Table S1 shows that Trz-PLPs (≤6% D-Trz) are characterized by a polydispersity index (PDI) that ranges from 0.08 ± 0.01 to 0.18 \pm 0.01, indicating that these particle preparations have a high degree of homogeneity (acceptable by pharmaceutical standards⁶⁰). For Trz-PLPs (≥10% D-Trz), the PDI ranges from 0.52 ± 0.05 to 0.25 ± 0.05 . This increase in PDI is often associated with particle heterogeneity and/or sample aggregation; however, we note that Zetasizer measurements were acquired in water, and low ionic strength conditions can promote particle self-association. No evidence of particle aggregation was observed by TEM, including particle preparations containing more than 6% D-Trz (Table S1, size). Additionally, no turbidity is observed for particles stored short-term in serum (24 h) or long-term in buffered solutions (>4 months) at 4 °C. Hence, the data suggest that higher ionic strength conditions are required for particle stability in liquid dispersions.

Given the inherent chemical properties of the gpD constructs, we anticipated an effect on overall particle charge. Indeed, this was qualitatively demonstrated by the altered migration of decorated particles during AGE (Figure 2A) and quantified by electrophoretic light scattering (ELS) analysis (Table S1, zeta potential (ZP)). Consistent with the presence

of negatively charged fluorescein molecules on the particle surface, F5M-PLPs are characterized by a ZP that decreases from -19.3 ± 0.3 mV to -26.8 ± 6.9 mV, as compared to WT PLPs (Table S1). For Trz-PLPs (0.5-30% D-Trz), the ZP ranges from -25.8 ± 0.7 mV to -6.0 ± 0.4 mV (Table S1). The increased positive charge is consistent with increasing the surface density of D-Trz on the particle surface (the isoelectric point of Trz, gpE, and gpD is 8.5, 5.3, and 5.5, respectively). Notably, factors such as particle charge have critical roles in particle-cell interactions: more cationic particles can lead to increased membrane destabilization, and a net positive particle surface charge aids in binding the negatively charged plasma membrane. 61 Therefore, we maintain an interest in characterizing how other molecules could influence the surface chemistry of lambda PLPs, which may elucidate other ways in which the platform can be manipulated to optimize certain biological responses.

Trz-PLPs Are Internalized by HER2⁺ Cells. A useful theranostic particle requires that biomolecules bound to the capsid surface remain functionally active; thus, to assess the functionality of chemically modified Trz (D-Trz), cell-based assays were employed using human breast carcinoma cell lines (SKBR3, HER2⁺ cells; MDA-MB-231, HER2⁻ cells). Each cell line was treated with 2 μ M free Trz or 2 nM Trz-PLPs (1% or 30% D-Trz). This was equivalent to either 291 μ g/mL free or 1.7 and 50.7 μ g/mL PLP-bound Trz. After 3 h at 37 °C, the cells were washed, fixed, and immunostained with Alexa Fluor

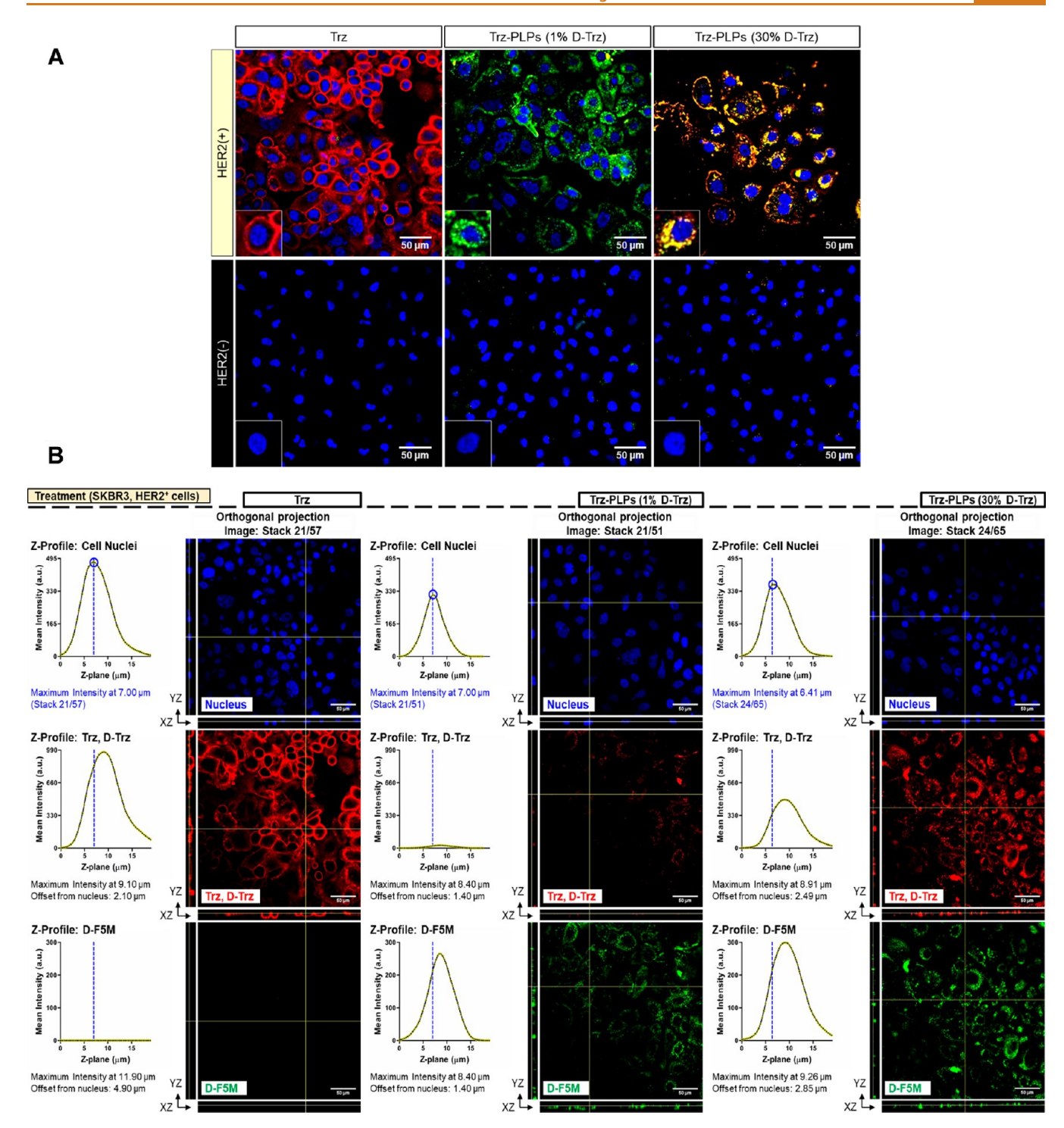


Figure 3. Trz-PLPs are internalized by breast cancer cells of the HER2 overexpression subtype. Confocal fluorescence microscopy was performed on breast cancer cells after treatment with 2 μ M free Trz or 2 nM Trz-PLPs (magnification, 40×; scale bars, 50 μ m), as described in Methods. Fluorescence signals: Trz and Trz-PLPs (red); cell nuclei (blue); Trz-PLPs (green). (A) Representative images of HER2⁺ cells (top) and HER2⁻ cells (bottom) after treatment captured at the median Z-plane of the nucleus and with the fluorescence signals merged (spectral overlap, yellow-orange). (B) Z-series were collected of treated cells, and the Z-profile was plotted to determine the optical section at which the fluorescent signal associated with the nucleus was maximal. Orthogonal projections were then generated to show cellular localization, as demonstrated by the X–Z and Y–Z projections shown at the bottom and to the left of the central representative image, respectively. The yellow line in the central image indicates the orthogonal planes of the X–Z and Y–Z projections.

594 anti-human IgG to visualize both free and chemically modified Trz (red). Cell nuclei were stained using Hoechst 33342 (blue); no staining was required for detection of Trz-PLPs due to the presence of D-F5M (green). Confocal fluorescence microscopy reveals that (i) neither Trz (free) nor

Trz-PLPs bind HER2⁻ cells at detectable levels; (ii) Trz binds to HER2⁺ cells and remains primarily localized to the plasma membrane; (iii) Trz-PLPs similarly bind HER2⁺ cells but are subsequently internalized to afford a punctate fluorescence pattern throughout the cell interior; (iv) merged fluorescence

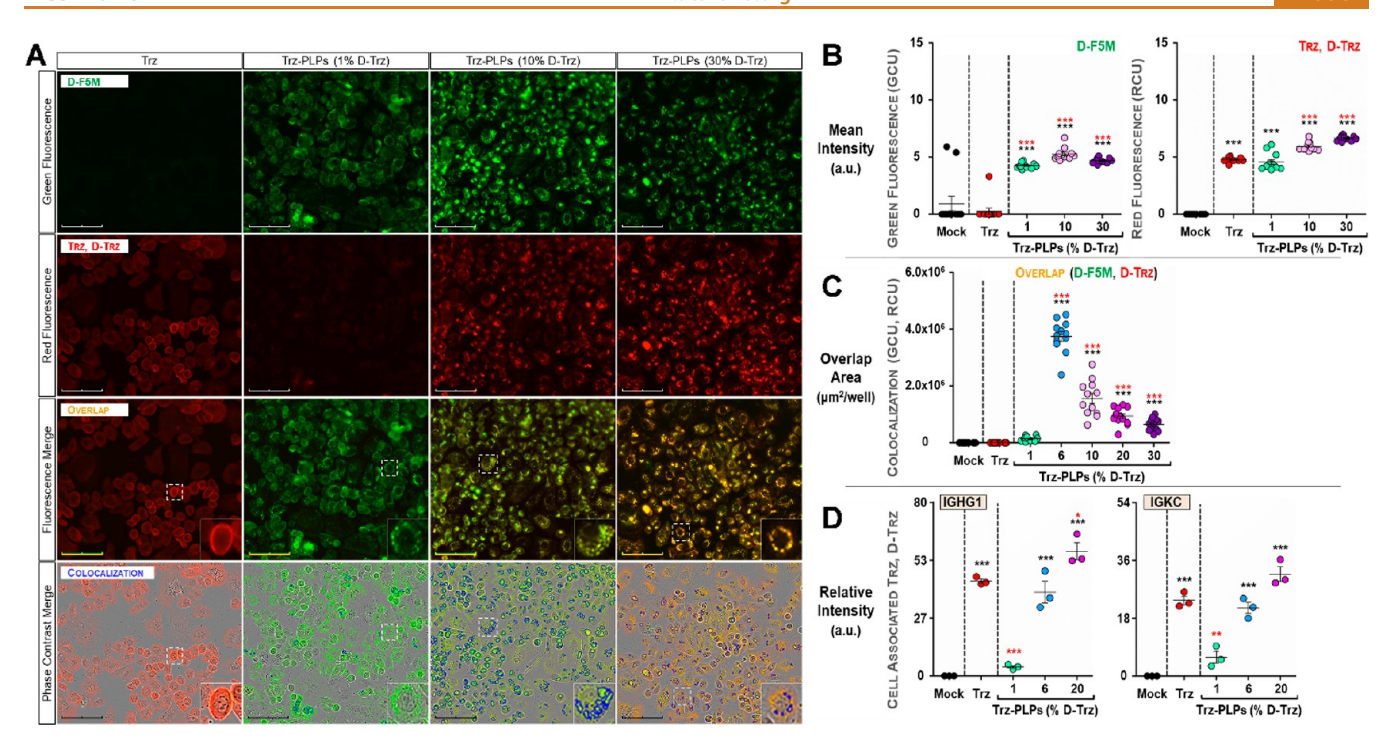


Figure 4. Trz-PLP internalization leads to an intracellular accumulation of D-Trz. (A–C) Incucyte system analysis of HER2 $^+$ cells treated with 2 μ M free Trz or 2 nM Trz-PLPs in 12 replicates. (A) High-throughput cell imaging was performed by the system prior to analysis (magnification, 40×; scale bars, 100 μ m). The rows for representative images show the following: (1) fluorescence signal from Trz-PLPs (green); (2) fluorescence signal from Trz and Trz-PLPs (red); (3) merged fluorescence signals (spectral overlap, yellow-orange); (4) merged fluorescence and phase contrast images with a mask (blue) applied to outline areas of spectral overlap. An enlarged view of a single cell is provided in the merged images (inset). (B) The mean intensity of fluorescence signals was quantified, and plots are shown for a subset of treatment groups (green, left; red, right). (C) The area of spectral overlap was quantified and plotted to compare colocalization of fluorescence signals across treatment groups. (D) Proteomics was conducted on HER2 $^+$ cells treated with 150 nM free Trz or 2 nM Trz-PLPs in triplicate. Levels of immunoglobulin constant regions were used to confirm the presence of Trz and D-Trz (IGHG1 protein (heavy chain), left; IGKC protein (light chain), right). For all plots (B)–(D), error bars are represented as \pm SEM derived from replicates. p-Values from a one-way repeated measures ANOVA, followed by a Dunnett's multiple comparison test, are shown as p < 0.05; **p < 0.01; ***p < 0.001. The control group in the Dunnett test (Mock/Trz) is denoted by a black or red asterisk, respectively.

images of HER2⁺ cells treated with Trz-PLPs suggest that D-F5M (green) and D-Trz (red) colocalize within the cell (spectral overlap, yellow-orange); and (v) increasing the surface density of D-Trz on Trz-PLPs correlates with increased intracellular levels of Trz (Figure 3). Control studies confirm that chemical modification of Trz does not alter its HER2 specificity or its cellular localization (Figure S2A). Additionally, F5M-PLPs do not appreciably interact with either cell line (even in the presence of Trz), nor do they affect the capacity of Trz to bind HER2 (Figure S2A). Lastly, both Trz and D-Trz strongly inhibit Trz-PLP internalization by HER2⁺ cells (Figure S2B), which indicates a competitive binding interaction. In summary, we conclude that Trz-PLPs specifically bind the HER2 receptor, and robust particle internalization requires physical association of Trz with the PLP surface.

Quantitative Assessment of Trz-PLP Internalization by HER2⁺ Cells. To quantify cellular uptake by HER2⁺ cells, we used an Incucyte system for automated image acquisition and analysis. This allowed for particle—cell interactions of a broader range of Trz-PLPs (0.5–30% D-Trz, equivalent to 0.8–50.7 μ g/mL PLP-bound Trz) to be interrogated in a more high-throughput manner. The data presented in Figures 4A and S3A reveal a similar fluorescence pattern to that observed by confocal microscopy, in which Trz is densely concentrated on the cell periphery but Trz-PLPs are distributed throughout

the cell. In support of the previous findings that the "dose" of Trz delivered to the cell interior can be regulated via shell surface functionalization, merged images show a fluorescence that transitions from green to yellow-orange as the surface density of D-Trz on Trz-PLPs is increased (Figures 4A, third row, and S3A). Additionally, while the levels of green fluorescence do not vary appreciably between particle types (all Trz-PLPs are decorated with 25% D-F5M), the levels of red fluorescence increase as a function of D-Trz surface density (Figure 4B). This corroborates an apparent intracellular accumulation of the modified biologic. A colocalization analysis was performed to calculate the area of spectral overlap for the two fluorescence signals, which suggests a high degree of colocalization in particle treatment groups containing ≥6% D-Trz (Figure 4C); refer to Figure S3B for fluorescence data reported in spectral counts.

As part of our omics approaches for characterizing the biological responses to Trz-PLPs (vide infra), proteomics data reveal the presence of immunoglobulin constant regions (heavy chain, IGHG1; light chain, IGKC) associated with HER2 $^+$ cells treated with either Trz or Trz-PLPs; refer to Table S2 for the full proteomics report and Figure S4 for data providing an overview of proteomics findings. Given that antibody constituents are not found in naïve cells and that Trz binds the HER2 receptor with high affinity ($K_{\rm D}$ 1.8–5 nM 40,62), the levels of these proteins provide a direct

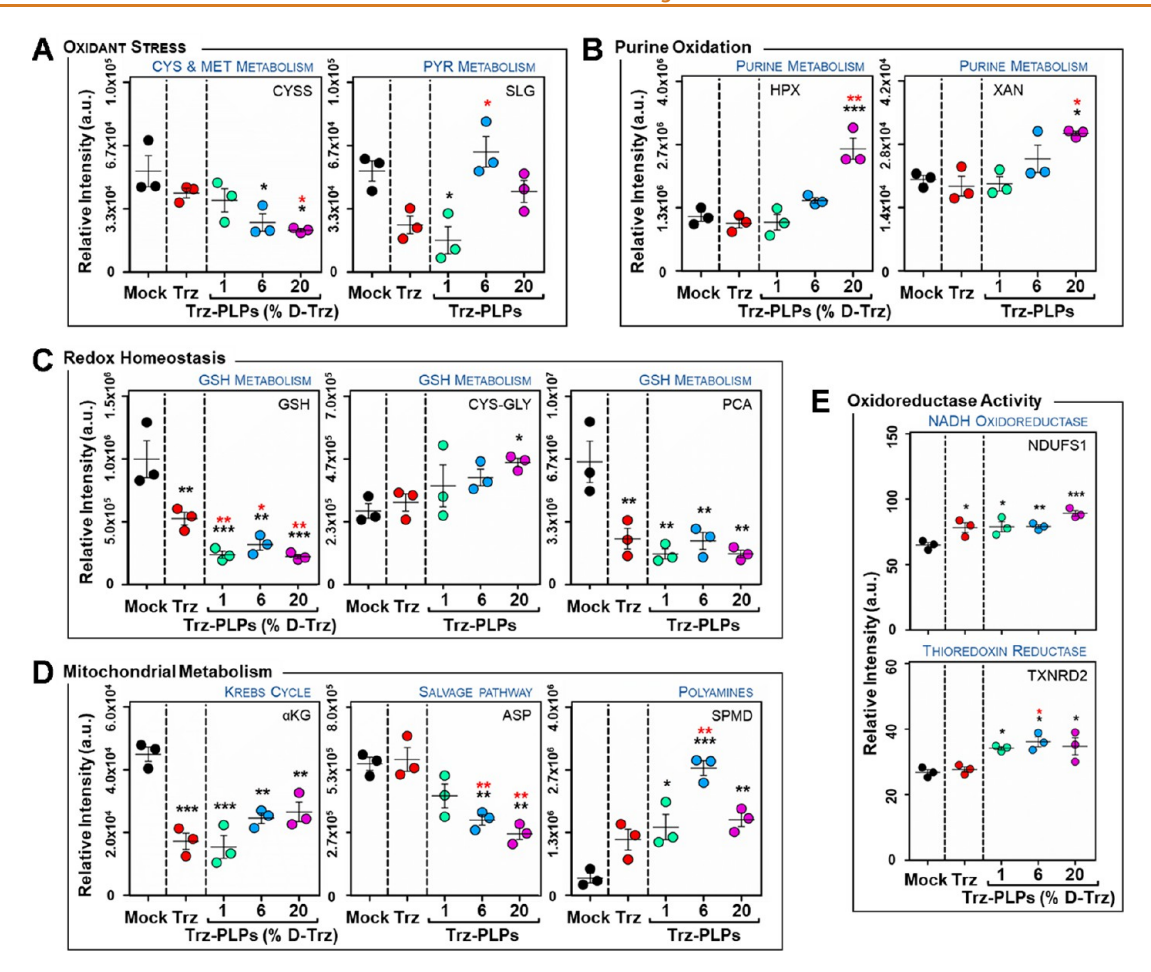


Figure 5. HER2-targeted treatment affects cellular redox potential. Metabolomics and proteomics were conducted on HER2 $^+$ cells treated with 150 nM free Trz or 2 nM Trz-PLPs. (A–D) Treatment impacts metabolites (black) belonging to multiple pathways (blue). These are associated with (A) oxidant stress regulation, (B, C) redox homeostasis, and (D) mitochondrial dysfunction. (E) Treatment impacts proteins (black) associated with oxidoreductase and NADP binding activity (blue). For all plots, the y-axis represents relative intensity (a.u.), and error bars are represented as \pm SEM derived from three replicates. p-Values from a one-way repeated measures ANOVA, followed by a Dunnett's multiple comparison test, are shown as *p < 0.05; **p < 0.01; ***p < 0.001. The control group in the Dunnett test (Mock/Trz) is denoted by a black or red asterisk, respectively. Refer to Table 1 for a summary of the statistical results (metabolites and proteins are listed by abbreviation, full name, and primary associated pathway).

measurement of the abundancy of Trz associated with HER2⁺ cells after treatment. Figure 4D demonstrates that the levels of cell-associated IGHG1 and IGKC increase as the surface density of D-Trz is increased on Trz-PLPs. In combination with the fluorescence data, we conclude that Trz-PLPs can be used for intracellular delivery of complex biologics (*e.g.*, antibodies) and that the delivered dose can be controlled by exterior modification of PLPs.

Trz-PLP Toxicity and Effects on Cellular Redox Homeostasis. We used two methodologies to evaluate the toxicity of PLP preparations on both HER2⁻ and HER2⁺ cells. First, a luminescent cytotoxicity assay was conducted to measure dead-cell protease activity due to the destabilization of the cellular membrane integrity upon death. Neither Trz, Naked PLPs, nor Trz-PLPs affect the viability of either cell line (Figure S5A). We next employed the MTT assay to measure effects on cellular viability due to metabolic perturbations of cellular NADH flux by NADH-dependent oxidoreductases. The metabolic activity of both cells lines is negatively affected by treatment with both free and PLP-bound Trz when the concentration of the biologic exceeds 16 μg/mL (Figure SSB).

To glean mechanistic insight on the effect on cellular metabolism for HER2+ cells, we characterized impacts to the metabolome and proteome after treatment with either Trz or Trz-PLPs; refer to Table S3 for a comprehensive metabolomics report and Figure S6 for an overview of metabolomics findings. For these experiments, the concentration of Trz was decreased to 20 µg/mL to better approximate the dose associated with Trz-PLPs (1%, 6%, and 20% D-Trz, equivalent to 1.7-33.8 μg/mL PLP-bound Trz). We focused on HER2⁺ cells since neither binding of the HER2 receptor nor particle internalization was detected in HER2⁻ cells. Metabolomics reveals that HER2-targeted treatment (i.e., treatment with either Trz or Trz-PLPs) affects amino acid and mitochondrial metabolism and causes dysregulation of redox homeostasis (Figures 5, S6, S7); refer to Table 1 for a summary of the statistical analysis and comparisons presented in Figure 5. Unlike Trz, Trz-PLPs result in increased levels of extracellular methionine, arginine, and ornithine and decreased intracellular levels of several amino acids related to mitochondrial function (threonine, asparagine, proline, serine) (Figures 5D, S7). Consistent with oxidant stress dysregulation, decreased levels of oxidized cysteine disulfide or S-lactoylglutathione are observed after

Table 1. Omics Summary for Figure 5

	Protein/Metabol	ite	Relative to Mock					Relative to Trz					
Abbr.	Name (Alt. name)	Pathway	ANOVA Dunnett's Multiple Comparison Test					ANOVA	ANOVA Dunnett's Multiple Comparison Tes				
			p-value	Treatment Group	Sig.	95% CI of Diff.	Mean	<i>p</i> -value	Treatment Group	Sig.	95% CI of Diff.	Mean	
CYSS	Cysteine disulfide (cystine)	CYS, MET metabolism	0.0209 (*)	Trz-PLPs (6% D-Trz) Trz-PLPs (20% D-Trz)	*	4.1e3 to 5.0e4 8.2e3 to 5.4e4	Lower Lower	0.0589 (ns)	Trz-PLPs (20% D-Trz)	*	72.3 to 3.9e4	Lower	
SLG	S-Lactoyl- glutathione	Pyruvate metabolism	0.0081 (**)	Trz-PLPs (1% D-Trz)	*	6.4e3 to 6.7e4	Lower	0.0159 (*)	Trz-PLPs (6% D-Trz)	*	-7.0e4 to -6.6e3	Higher	
HPX	Hypoxanthine	Purine metabolism	0.0005 (***)	Trz-PLPs (20% D-Trz)	***	-2.1e6 to -7.6e5	Higher	0.0019 (**)	Trz-PLPs (20% D-Trz)	**	-2.3e6 to -8.2e5	Higher	
XAN	Xanthine	Purine metabolism	0.0127 (*)	Trz-PLPs (20% D-Trz)	*	-1.9e4 to -1.9e3	Higher	0.0198 (*)	Trz-PLPs (20% D-Trz)	*	-2.1e4 to -2.8e3	Higher	
GSH	Reduced glutathione	Glutathione metabolism		Trz Trz-PLPs (1% D-Trz) Trz-PLPs (6% D-Trz) Trz-PLPs (20% D-Trz)	**	1.3e5 to 8.1e5 4.2e5 to 1.1e6 3.4e5 to 1.0e6 4.4e5 to 1.1e6	Lower Lower Lower Lower	0.0056 (**)	Trz-PLPs (1% D-Trz) Trz-PLPs (6% D-Trz) Trz-PLPs (20% D-Trz)	**	1.1e4 to 4.6e5 3.4e4 to 3.8e5 1.3e5 to 4.8e5	Lower Lower Lower	
CYS-GLY	Cysteinylglycine	Glutathione metabolism	0.0748 (ns)	Trz-PLPs (20% D-Trz)	*	-3.5e5 to -8.3e3	Higher	0.2477 (ns)	-	-	-	-	
PCA	Pyroglutamate (5-oxoproline)	Krebs Cycle		Trz Trz-PLPs (1% D-Trz) Trz-PLPs (6% D-Trz) Trz-PLPs (20% D-Trz)	**	1.5e6 to 6.7e6 2.3e6 to 7.5e6 1.6e6 to 6.8e6 2.3e6 to 7.5e6	Lower Lower Lower Lower	0.4689 (ns)	-	-	-	-	
αKG	alpha- Ketoglutarate (2- oxoglutarate)	Krebs Cycle		Trz Trz-PLPs (1% D-Trz) Trz-PLPs (6% D-Trz) Trz-PLPs (20% D-Trz)	***	1.6e4 to 4.0e4 1.8e4 to 4.1e4 8.4e3 to 3.2e4 6.5e3 to 4.0e4	Lower Lower Lower Lower	0.0456 (*)	-	-	-	-	
ASP	Aspartate	Amino acid metabolism	0.0016 (**)	Trz-PLPs (6% D-Trz) Trz-PLPs (20% D-Trz)	**	7.0e4 to 4.1e5 1.3e5 to 4.7e5	Lower Lower	0.0055 (**)	Trz-PLPs (6% D-Trz) Trz-PLPs (20% D-Trz)	**	8.6e4 to 4.3e5 1.4e5 to 4.9e5	Lower Lower	
SPMD	Spermidine	Polyamine biosynthesis	0.0005 (***)	Trz-PLPs (1% D-Trz) Trz-PLPs (6% D-Trz) Trz-PLPs (20% D-Trz)	* ***	-1.9e6 to -2.2e5 -3.2e6 to -1.5e6 -2.1e6 to -3.8e5	Higher Higher Higher	0.0131	Trz-PLPs (6% D-Trz)	**	-2.5e6 to -5.3e5	Higher	
NDUFS1	NADH-ubiquinone oxidoreductase 75 kDa subunit	Respiratory electron transport (mitochondrial)		Trz Trz-PLPs (1% D-Trz) Trz-PLPs (6% D-Trz) Trz-PLPs (20% D-Trz)	* ** **	-23.7 to -3.1 -24.4 to -3.8 -24.6 to -3.9 -34.6 to -14.0	Higher Higher Higher Higher	0.0885 (ns)	-	-	-	-	
TXNRD2	Thioredoxin reductase 2	Detoxification of ROS	0.0086 (**)	Trz-PLPs (1% D-Trz) Trz-PLPs (6% D-Trz) Trz-PLPs (20% D-Trz)	* *	-14.2 to -0.6 -16.1 to -2.5 -14.8 to -1.1	Higher Higher Higher	0.0609 (ns)	Trz-PLPs (6% D-Trz)	*	-16.3 to -0.5	Higher	

treatment with Trz-PLPs (6% and 20% D-Trz) or Trz-PLPs (1% D-Trz), respectively (Figure 5A). Trz-PLPs (20% D-Trz) also result in increased levels of cysteinylglycine and purine oxidation products (hypoxanthine, xanthine, inosine, adenosine), indicative of dysregulated redox homeostasis (Figures 5B, S6E). Impaired redox regulation is further supported by depletions of glutathione and decreased levels of pyroglutamate and methionine following HER2-targeted treatment (Figures 5C, S7A). Only Trz-PLP treatment results in decreased levels of glycine and glutamine (Figure S7B), whereas treatment with either Trz or Trz-PLPs causes decreases to the levels of aspartate, α -ketoglutarate, and oxaloacetate but increases in polyamines, such as spermidine, a marker of mitochondrial dysfunction following oxidant stress⁶⁵ (Figures 5D, S6E). Of note, glycine, glutamine, and aspartate are associated with purine oxidation and mitochondrial function by serving as carbon and nitrogen donors for purine biosynthesis⁶⁶ or through salvage of deaminated purines⁶⁷ and use as alternative fuels for mitochondrial metabolism.⁶⁸ Metabolic findings are supported by increased levels of thioredoxin reductase 2 and the mitochondrial NADHubiquinone oxidoreductase 75 kDa subunit from the proteomics data (Figure 5E). In summary, we conclude that cellular redox homeostasis, which is essential for the maintenance of cellular processes such as signal transduction, mechanisms for regulating reactive oxygen species (ROS), and cell proliferation, is affected by Trz-PLPs in ways that are both similar and unique to responses elicited by Trz.

Trz-PLPs Inhibit Proliferation of HER2⁺ Cells. Members of the HER family are receptor tyrosine kinases (RTKs) that lead to extensive downstream signaling to promote diverse cellular programs. Of note, overexpression of HER2 is implicated in the dysregulation of HER-mediated cell responses, 69 including cell proliferation, endocytic internalization, and endosomal sorting. Having ascertained that D-Trz retains biological activity, we next sought to determine whether Trz-PLPs could inhibit cell proliferation as observed with Trz. 40 Since Trz-PLPs are internalized, we hypothesized that inhibitory effects would be prolonged relative to Trz. To test this hypothesis, cell proliferation was examined following exposure to a single dose of Trz or Trz-PLPs, as described in Methods. Briefly, HER2⁺ cells were treated with Trz (20 μ g/ mL, free Trz) or Trz-PLPs (1.7–50.7 μg/mL, PLP-bound Trz) for 3 h and then harvested and cultured in the absence of Trz for 9 days. After 3 days postexposure, Trz-PLPs (10% and 30% D-Trz) achieved higher levels of growth inhibition (68% and 75%, respectively) versus Trz alone (54%) (Figures 6A, S8). After 6 days postexposure, Trz-PLPs (6-30% D-Trz) caused a 61–76% decrease in cell proliferation, whereas Trz resulted in only a 42% reduction (Figures 6A,B and S8). Notably, cells treated with Trz fully recover by 9 days postexposure, while the Trz-PLP treatment groups retain an inhibitory phenotype (Figures 6A,B and S8).

The proliferation data for 9 days postexposure reveal that the inhibitory phenotypes for cells treated with lambda PLPs cluster into two groups, which we designate as cluster 1 and

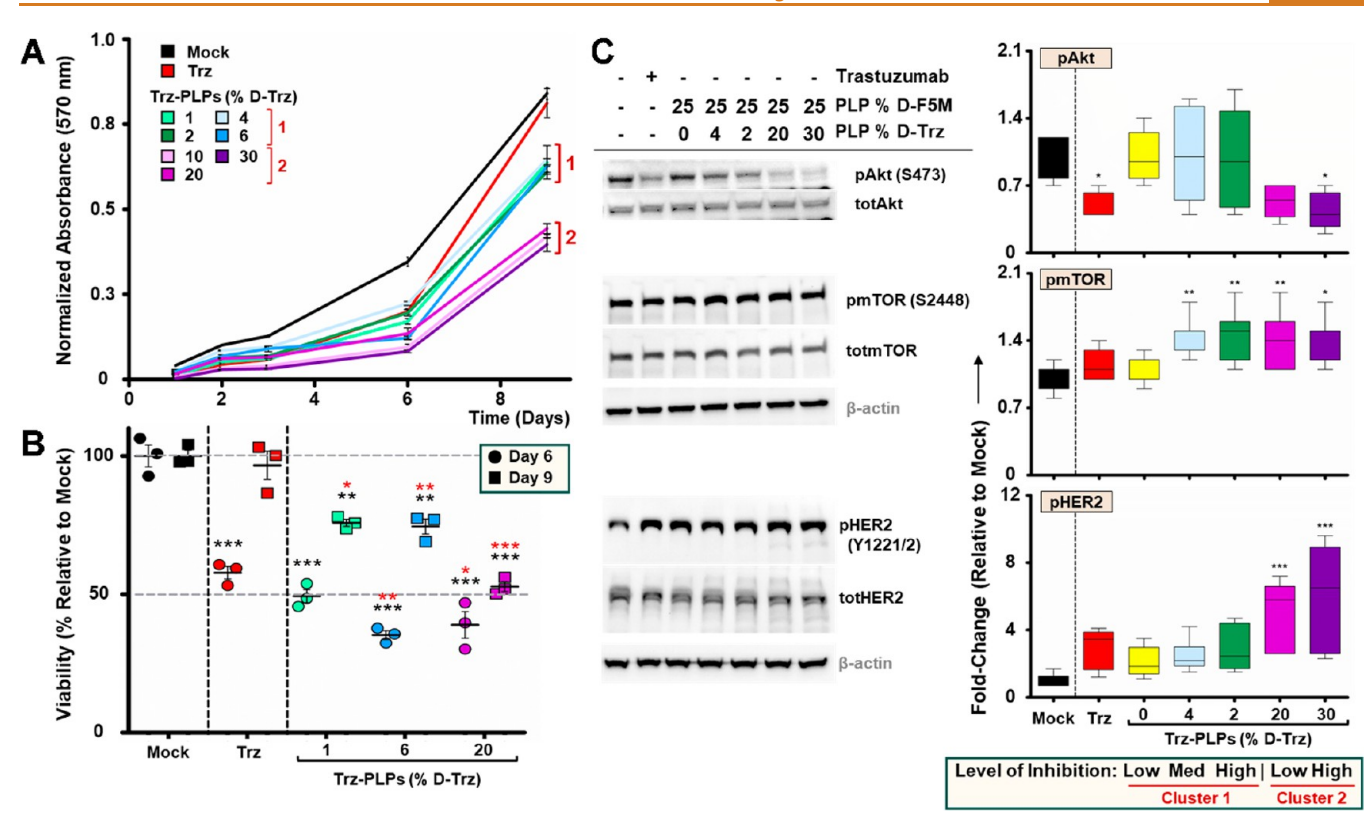


Figure 6. Trz-PLPs affect cellular proliferation and HER2 signaling. HER2⁺ cells were treated with 150 nM free Trz or 2 nM Trz-PLPs. (A, B) Cells were harvested, replated, and cultured in the absence of Trz (free or PLP-bound). (A) Proliferation was assessed over 9 days by crystal violet staining. Data shown are an average of three independent experiments done in triplicate with absorbance values normalized to 1. Error bars are represented as \pm SEM. Inhibitory effects are modulated as a function of PLP-bound Trz and fall into two clusters (bracketed and numbered, red). (B) Optical density values for days 6 and 9 were converted into percentages relative to Mock. (C) Representative Western blots of HER2⁺ cells treated for 3 h (left). Quantification of representative blots was done using a Bio-Rad gel imaging system (right). All proteins were first normalized to the loading control (β -actin, gray). Phosphorylation levels were then estimated by normalizing the phosphorylation densities to their respective total. Data shown are an average of three independent experiments done in duplicate with error bars represented as \pm SEM. Trz-PLPs are ordered according to level of inhibition (low/medium/high) based on the group average percentage of inhibition. p-Values from a one-way repeated measures ANOVA, followed by a Dunnett's multiple comparison test, are shown as $p \leq 0.05$; ** $p \leq 0.01$; *** $p \leq 0.001$. The control group in the Dunnett test (Mock/Trz) is denoted by a black or red asterisk, respectively.

cluster 2 (Figures 6A, S8A). Trz-PLPs (1–6% D-Trz) fall into cluster 1 and cause a 25% group average decrease in cell proliferation (Figures 6A, S8). Unexpectedly, WT PLPs and F5M-PLPs also belong to cluster 1 and result in a 20% group average inhibition (Figure S8A). This suggests that another mechanism is contributing to the cell growth inhibition mediated by lambda PLPs due to particle—cell interactions independent of HER2. Cluster 2 includes Trz-PLPs (10–30% D-Trz) and results in 50% average inhibition (Figures 6A,B and S8). These results indicate that cellular uptake of Trz-PLPs increases the durability of the inhibitory response and demonstrate that Trz-PLPs (10–30% D-Trz) can inhibit cell growth more significantly than Trz.

Studies show that HER2 internalization depends on antibody-induced HER2 clustering;⁷⁰ for example, Trz must be used in combination with two or more noncompetitive antibodies for efficient HER2 internalization.^{71,72} Additionally, the surface density of the target receptor on a cell of interest is critical for effective retention of a nanoparticle due to receptor engagement.⁷³ Therefore, we hypothesize that robust Trz-PLP internalization by cells overexpressing HER2 results from multipartite interactions provided by the presentation of multiple copies of Trz on the particle surface with multiple

HER2 receptors on the cell surface (avidity effect). These interactions would prolong Trz-PLP retention and contribute to the biological responses observed, including the more durable growth inhibition phenotype. Future studies interrogating the mechanisms of cellular uptake will be necessary to better define the contributions of internalization pathways for trafficking of Trz-PLPs.

Disruption of HER2 Signaling and Associated Pathways. The mechanism of action for Trz is complex;⁷⁴ however, the primary effect on HER2 signaling is the suppression of the Ras/Raf/MAPK and PI3K/Akt/mTOR pathways to thereby inhibit cell-cycle progression and sensitize cells to DNA damage. 75,76 Thus, we examined the effect of Trz-PLP treatment in HER2+ cells, focusing on three key kinases (Akt, mTOR, HER2). Figure 6C demonstrates that treatment with Trz-PLPs (20% and 30% D-Trz), which belong to cluster 2 of the cell proliferation data, causes a 46-55% decrease in Akt phosphorylation at Ser473, similar to treatment with Trz (51% decrease); no significant effect is observed for particles belonging to cluster 1. Given that Rictor and Sin1 (components of mTORC2) are essential for phosphorylation of Akt at Ser473,⁷⁷ these proteins could be contributing to the effects on cell proliferation and amino acid metabolism

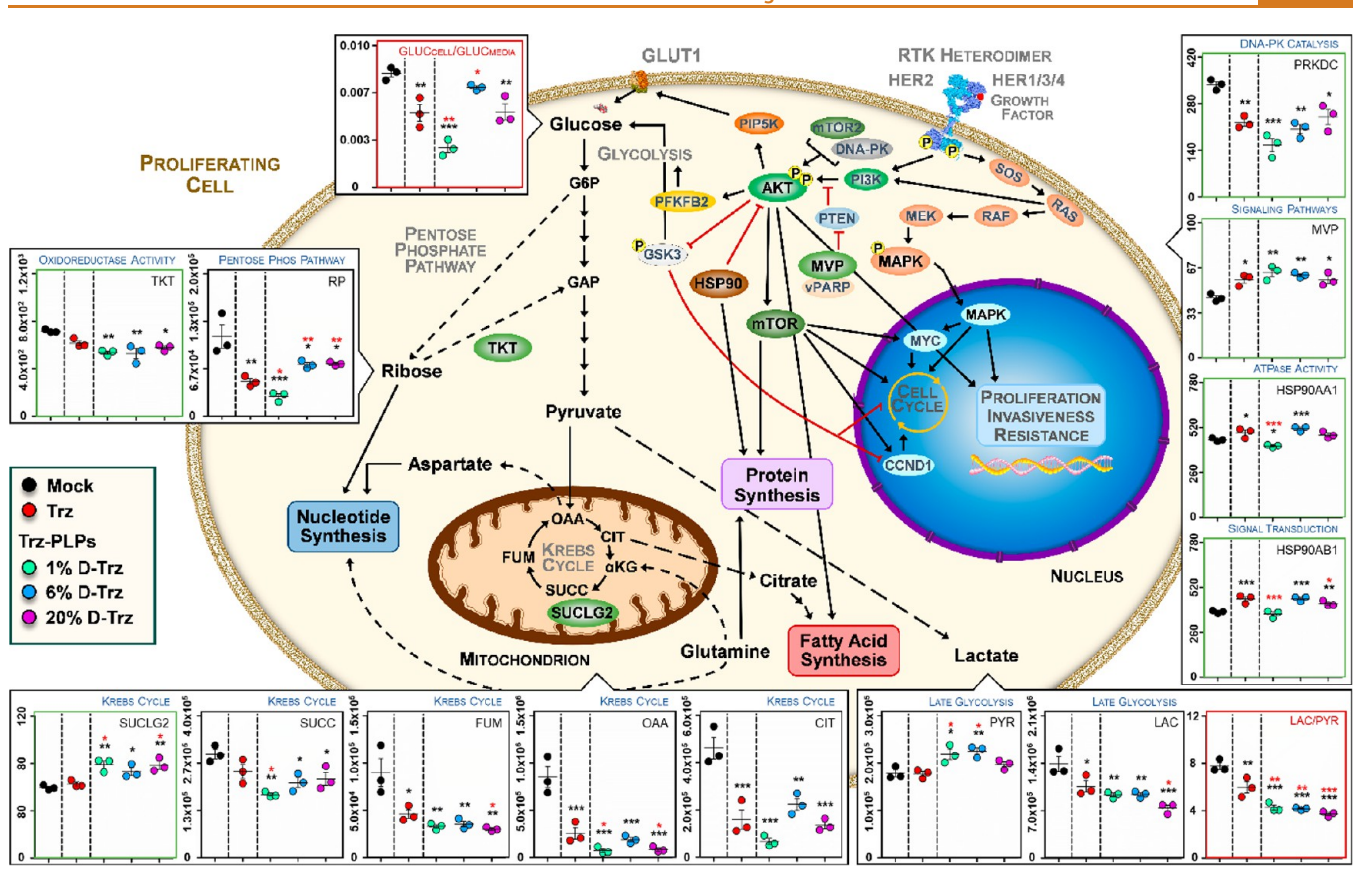


Figure 7. HER2-targeted treatment alters cellular programs. Activated HER receptors (RTK dimers) recruit cascades of signaling molecules to promote diverse cellular programs, and the PI3K/Akt/mTOR signaling axis serves as a key regulator of metabolic pathways that are altered in cancer cells to meet the higher demands of precursors for protein, nucleotide, and fatty acid synthesis. Metabolomics and proteomics of HER2+ cells reveal several changes to key biological processes (blue text), metabolites (black text, box; ratios, red text, box), and proteins (black text, green box) after treatment with Trz or Trz-PLPs. For all plots, the y-axis and error bars represent relative intensity (a.u.) and \pm SEM derived from three replicates, respectively. p-Values from a one-way repeated measures ANOVA, followed by a Dunnett's multiple comparison test, are shown as $*p \le 0.05$; $**p \le 0.01$; $***p \le 0.001$. Refer to Table 2 for a summary of the statistical results.

mediated by these particles (Figures 6A,B and S6). Additionally, only Trz-PLP treatment has an effect on mTOR, causing up to a 39% increase in mTOR phosphorylation at Ser2448; no effect is observed for Trz or F5M-PLP treatment (Figure 6C). Given that Trz-PLPs impact amino acid metabolism (Figure S6), it is possible that higher levels of mTOR phosphorylation could be attributed to S6K (p70S6), the S2448 kinase whose activity is modulated by the cellular amino acid status via the TSC/Rheb pathway.⁷⁸ Lastly, treatment with particles belonging to cluster 2 results in increased HER2 phosphorylation at Tyr1221/1222; no effect is observed for treatments with Trz or particles belonging to cluster 1 (Figure 6C). Phosphorylation at this site couples HER2 to the Ras/ Raf/MAP kinase pathway, which presents a potential compensatory mechanism for promoting cell growth in the absence of Akt activation. Overall, these findings confirm that Trz-PLPs can influence the activity of important enzymes in the PI3K/Akt/mTOR pathway.

Trz-PLPs Alter the Metabolomic and Proteomic Landscapes of HER2⁺ Cells. While the correlation between metabolic derangement and *HER2* amplification is well established^{80,81} and can be influenced by HER2-targeted therapies, ⁸² this study demonstrates ways in which the lambda PLP platform can be utilized to alter cellular programs. Omics approaches were taken to establish a connection between HER2-mediated activation of the PI3K/Akt/mTOR pathway

and effects on associated cellular pathways, such as glycolysis, the pentose phosphate pathway, the Krebs cycle, and the synthesis of proteins, nucleotides, and fatty acids. HER2-targeted treatment results in decreased levels of most Krebs cycle metabolites, but only Trz-PLPs cause a decrease in the level of succinate and an increase in the level of the mitochondrial subunit of succinyl-CoA synthase (Figure 7, Table 2). Of note, succinyl-CoA synthase couples the hydrolysis of succinyl-CoA to GTP synthesis, ⁸³ catalyzing the only step of substrate-level phosphorylation in the Krebs cycle. These changes could directly impact intracellular redox homeostasis by affecting the cell's ability to replenish intracellular pools of GSH and NADPH that are heavily dependent on the Krebs cycle.

Cancer cells rely heavily on the pentose phosphate pathway to survive increased oxidant stress and promote growth. As a compensatory response, this pathway is enhanced to yield high levels of NADPH for redox regulation and fatty acid synthesis and ribose phosphate (RP) for nucleotide synthesis. HER2-targeted treatment results in decreased levels of RP and lactate, but only Trz-PLPs cause a decrease in the levels of transketolase (TKT) and an increase in the levels of pyruvate (Figure 7, Table 2). TKT links RP to glycolysis (aids in regulating glucose import) and is associated with the sensitization of tumor and cancer cells to oxidative stress. A4,86 Therefore, diminished cellular levels of RP and TKT could aid

Table 2. Omics Summary for Figure 7

Protein/Metabolite			Relative to Mock						Relative to Trz					
			ANOVA Dunnett's Multiple Comparison Test					ANOVA	ANOVA Dunnett's Multiple Comparison					
Abbr.	Name	Pathway	<i>p</i> -value	Treatment Group	Sig.	95% CI of Diff.	Mean	p-value	Treatment Group	Sig.	95% CI of Diff.	Mean		
GLUC _{cell} / GLUC _{media}	Ratio of extra- to intra-cellular glucose	Glycolysis	< 0.0001 (***)	Trz Trz-PLPs (1% D-Trz) Trz-PLPs (20% D-Trz)	** ***	0.001 to 0.004 0.004 to 0.007 0.001 to 0.004	Lower Lower Lower	0.0004 (***)	Trz-PLPs (1% D-Trz) Trz-PLPs (6% D-Trz)	**	0.001 to 0.004 -0.003 to 0.0	Lower Higher		
TKT	Transketolase	Pentose phosphate pathway	0.0036 (**)	Trz-PLPs (1% D-Trz) Trz-PLPs (6% D-Trz) Trz-PLPs (20% D-Trz)	**	75.5 to 2.9e2 83.9 to 2.9e2 34.9 to 2.5e2	Lower Lower Lower	0.1972 (ns)	-	=	-	-		
RP	Ribose phosphate	Pentose phosphate pathway	0.0010 (**)	Trz Trz-PLPs (1% D-Trz) Trz-PLPs (6% D-Trz) Trz-PLPs (20% D-Trz)	** *	2.8e4 to 9.9e4 4.9e4 to 1.2e5 4.1e3 to 7.5e4 3.0e3 to 7.4e4	Lower Lower Lower Lower	0.0003 (***)	Trz-PLPs (1% D-Trz) Trz-PLPs (6% D-Trz) Trz-PLPs (20% D-Trz)	* **	5.4e3 to 3.6e4 -3.9e4 to -8.2e3 -4.0e4 to -9.4e3	Lower Higher Higher		
SUCLG2	Succinyl-CoA synthetase, β-subunit	Krebs Cycle	0.0015 (**)	Trz-PLPs (1% D-Trz) Trz-PLPs (6% D-Trz) Trz-PLPs (20% D-Trz)	**	-30.2 to -8.6 -24.4 to -2.8 -29.8 to -8.2	Higher Higher Higher	0.0206 (*)	Trz-PLPs (1% D-Trz) Trz-PLPs (20% D-Trz)	*	-28.8 to -3.9 -28.3 to -3.5	Higher Higher		
SUCC	Succinate	Krebs Cycle	0.0058 (**)	Trz-PLPs (1% D-Trz) Trz-PLPs (6% D-Trz) Trz-PLPs (20% D-Trz)	**	5.2e4 to 1.8e5 1.7e4 to 1.4e5 7.3e3 to 1.3e5	Lower Lower Lower	0.0686 (ns)	Trz-PLPs (1% D-Trz)	*	5.9e3 to 1.2e5	Lower		
FUM	Fumarate	Krebs Cycle	0.0024 (**)	Trz Trz-PLPs (1% D-Trz) Trz-PLPs (6% D-Trz) Trz-PLPs (20% D-Trz)	**	1.2e4 to 7.6e4 2.5e4 to 8.9e4 2.6e4 to 8.6e4 2.8e4 to 9.2e4	Lower Lower Lower Lower	0.0533 (ns)	Trz-PLPs (20% D-Trz)	*	1.8e3 to 3.0e4	Lower		
OAA	Oxaloacetate	Krebs Cycle	0.0002 (***)	Trz Trz-PLPs (1% D-Trz) Trz-PLPs (6% D-Trz) Trz-PLPs (20% D-Trz)	*** *** ***	3.2e5 to 8.8e5 5.0e5 to 1.1e6 3.8e5 to 9.4e5 4.9e5 to 1.1e6	Lower Lower Lower Lower	0.0253 (*)	Trz-PLPs (1% D-Trz) Trz-PLPs (20% D-Trz)	*	3.3e4 to 3.3e5 2.1e4 to 3.2e5	Higher Higher		
CIT	Citrate	Krebs Cycle	0.0003 (***)	Trz Trz-PLPs (1% D-Trz) Trz-PLPs (6% D-Trz) Trz-PLPs (20% D-Trz)	*** ***	1.6e5 to 4.5e5 2.5e5 to 5.4e5 9.5e4 to 3.8e5 1.8e4 to 4.7e5	Lower Lower Lower Lower	0.0305	-	-	-	-		
PYR	Pyruvate	Glycolysis	0.0034 (**)	Trz-PLPs (1% D-Trz) Trz-PLPs (6% D-Trz)	*	-7.0e4 to -1.0e4 -7.6e4 to -1.7e4	Higher Higher	0.0171 (*)	Trz-PLPs (1% D-Trz) Trz-PLPs (6% D-Trz)	*	-7.4e4 to -6.9e3 -8.1e4 to -1.4e4	Higher Higher		
LAC	Lactate	Glycolysis	0.0028 (**)	Trz Trz-PLPs (1% D-Trz) Trz-PLPs (6% D-Trz) Trz-PLPs (20% D-Trz)	***	1.5e4 to 6.5e5 1.4e5 to 7.8e5 1.3e5 to 7.7e5 3.3e4 to 9.7e5	Lower Lower Lower Lower	0.0287 (*)	Trz-PLPs (20% D-Trz)	*	8.7e4 to 5.5e5	Lower		
LAC/PYR	Ratio of intracellular PYR to LAC	Glycolysis	< 0.0001 (***)	Trz Trz-PLPS (1% D-Trz) Trz-PLPs (6% D-Trz) Trz-PLPs (20% D-Trz	** *** ***	0.605 to 3.0 2.3 to 4.7 2.4 to 4.8 2.8 to 5.2	Lower Lower Lower Lower	0.0013 (**)	Trz-PLPs (1% D-Trz) Trz-PLPs (6% D-Trz) Trz-PLPs (20% D-Trz)	**	0.756 to 2.6 0.865 to 2.7 1.3 to 3.1	Lower Lower Lower		
HSP90AA1	Heat shock protein, α-isoform	Signaling pathways	0.0001 (***)	Trz Trz-PLPs (1% D-Trz) Trz-PLPs (6% D-Trz)	* **	-71.4 to -8.0 4.9 to 68.3 -96.3 to -32.9	Higher Lower Higher	0.0002 (***)	Trz-PLPs (1% D-Trz)	***	46.9 to 1.1e2	Lower		
HSP90AB1	Heat shock protein, β-isoform	Signal transduction	< 0.0001 (***)	Trz Trz-PLPs (6% D-Trz) Trz-PLPs (20% D-Trz)	*** ***	-1.1e2 to -42.1 -1.1e2 to -43.8 -78.2 to -14.7	Higher Higher Higher	0.0002 (***)	Trz-PLPs (1% D-Trz) Trz-PLPs (20% D-Trz)	***	58.9 to 1.1e2 0.452 to 54.3	Lower Lower		
MVP	Major vault protein	Signaling pathways	0.0047 (**)	Trz Trz-PLPs (1% D-Trz) Trz-PLPs (6% D-Trz) Trz-PLPs (20% D-Trz)	* ** ** *	-23.8 to -3.0 -29.1 to -8.3 -27.1 to -6.2 -23.8 to -3.0	Higher Higher Higher Higher	0.4922 (ns)	-	-	-	-		
PRKDC	DNA-PK, catalytic subunit	DNA-PK catalysis	0.0009 (***)	Trz Trz-PLPs (1% D-Trz) Trz-PLPs (6% D-Trz) Trz-PLPs (20% D-Trz)	** **	39.4 to 1.9e2 1.1e2 to 2.6e2 59.6 to 2.1e2 23.0 to 1.7e2	Lower Lower Lower Lower	0.0855 (ns)	-	-	-	-		

in the sensitization of HER2⁺ cells to reactive intermediates and decrease their capacity to repair DNA damage. Consistent with limiting the tolerance of cancer cells to DNA damage, decreased levels of the DNA-dependent protein kinase catalytic subunit (PRKDC) are observed following HER2 treatment (Figure 7, Table 2). This could, in part, explain the

impaired phosphorylation of Akt at S473 (Figure 6C), since phosphorylation of Akt at this site can be mediated by DNA-dependent protein kinase in response to DNA damage.⁸⁷ Increased levels of heat-shock protein 90 (HSP90) isoforms and the major vault protein (MVP) (Figure 7, Table 2) could also lead to decreased Akt phosphorylation *via* modulation of

PI3K activity. 87,88 Given the changes to HSP90, Trz-PLPs could have a role in the regulation of HER2 turnover, since HER2 (unlike the other HER proteins but also true for Akt) remains in complex with HSP90 upon maturation and HSP90 inhibitors induce degradation of HER2.

Lastly, Trz-PLPs (>6% D-Trz) result in substantial accumulations of IMP, adenosine, and hypoxanthine, essential metabolites in purine biosynthesis and, by extension, cell growth. Studies assessing the enzymatic activity of phosphoribosyl pyrophosphate, aminoimidazole-carboxamide ribonucleoside, and hypoxanthine phosphoribosyl transferase could validate whether Trz-PLPs are acting as an antipurine. Additional studies, including experiments performed *in vivo* with transcriptional and flow cytometric data, are required to elucidate the precise mechanisms by which Trz-PLPs are eliciting these changes and to confirm the apparent regulation of gene products identified from our proteomics analysis. Nevertheless, the data demonstrate that Trz-PLPs can alter cellular programs related to cancer progression at a functional level.

CONCLUSION

In this study, we constructed PLPs simultaneously decorated with a fluorescent probe and various surface densities of a therapeutic antibody and characterized their physiochemical properties. We demonstrated that D-F5M can be used to efficiently track particles in vitro, and D-Trz retains the same biological activity as native Trz. Trz-PLPs are robustly internalized by HER2+ cells, which allows the intracellular dose of trastuzumab to be regulated by varying the amount of D-Trz on the particle surface. The increased intracellular concentrations of the biologic in combination with extensive effects on cellular programs result in a durable and expanded biological response that is distinct from treatment with Trz. Notably, inhibition of cell growth does not require continuous exposure to the therapeutic, which suggests that the propensity of cancer cells to develop trastuzumab resistance could be reduced.

Cancer cells are remarkably dynamic in their ability to regulate cellular processes for their growth and survival. Trz-PLP "rewiring" of HER2⁺ cells appears to be synergistic in that several pathways associated with cell proliferation are impacted, demonstrating the utility of lambda PLPs as a platform to interrogate the regulation of several cellular processes (e.g., proliferation, metabolism, oncogenic signaling) and the mechanisms by which cancer cells may develop drug resistance. Further, this study reveals the potential of Trz-PLPs as a therapeutic agent, setting the stage for future studies aimed at evaluating the platform in the context of complex tumor microenvironments and in vivo. Importantly, the platform can be readily adapted in a user-defined manner with additional or other biologics for specific targeting of other cell receptors (e.g., cetuximab for targeting HER1), for controlled intracellular delivery of regulatory or toxic biologics (e.g., adotrastuzumab emtansine (Kadcyla; Genentech), enzyme inhibitors, chemotherapeutic drugs) and to improve drug metabolism/pharmacokinetic (DMPK) properties in vivo (e.g., incorporation of synthetic polymers).

METHODS

Materials and Methods. Amicon centrifugal filters were purchased from Sigma-Aldrich (St. Louis, MO, USA). HiTrapQ HP, HiTrapSP. and Superose 6 Increase columns were purchased

from GE Healthcare (Marlborough, MA, USA). Zeba spin desalting columns, fluorescein-5-maleimide, Hoechst 33342, protease and phosphatase inhibitor cocktail, Corning vacuum filters, 96-well plates, and Nunc Lab-Tek eight-chambered glass slides (#1.0 borosilicate) were purchased from Thermo Fisher Scientific (San Jose, CA, USA). Maleimide polyethylene glycol succinimidyl valerate (Mal-PEG-VA, 3.4k $M_{\rm n}$) was purchased from Laysan Bio, Inc. (Arab, AL, USA). Alexa Fluor 594 AffiniPure goat anti-human IgG was purchased from Jackson ImmunoResearch Laboratories, Inc. (West Grove, PA, USA). All antibodies used for immunoblotting were purchased from Cell Signaling Technology (Beverly, MA, USA). All other materials were of the highest quality commercially available.

All protein purifications utilized an ÄKTA purifier chromatography system (GE Healthcare). Absorbance spectra were obtained using a Thermo Scientific NanoDrop UV—vis spectrophotometer.

PLP Purification. Lambda PLPs were expressed in E. coli BL21(DE3)[pNu3_E] cells and purified, as described^{20,89} with modification. Concentrations of lysozyme (0.4 mg/mL) and DNase (0.04 mg/mL) in cell lysates were increased to improve protein extraction efficiency. Following rate-zonal, 10-40% sucrose density gradient ultracentrifugation, PLPs were collected from the third band, concentrated, and exchanged into 20 mM Tris [pH 8.0, 4 °C] buffer containing 15 mM MgCl₂, 1 mM EDTA, and 7 mM β -ME using Amicon centrifugal filter units (100k MWCO). Proteins were fractionated by anion exchange chromatography employing three 5 mL HiTrap Q HP columns connected in tandem and developed with a 30-column volume linear gradient to 1 M NaCl. The eluate was analyzed by denaturing SDS-PAGE, and PLP-containing fractions were pooled, exchanged into 50 mM HEPES [pH 7.4] buffer containing 100 mM NaCl and 10 mM MgCl₂, and stored at 4 °C until further use.

Purification of gpD Proteins. Wild-type gpD and gpD(S42C) were expressed in E. coli BL21(DE3)[pD] and BL21(DE3)-[pDS542C] cells, respectively, and purified, as previously described^{20,89} with modification. Concentrations of lysozyme (0.4 mg/ mL) and DNase (0.04 mg/mL) in cell lysates were increased, and lysate supernatants were dialyzed overnight against 20 mM Tris [pH 8.0, 4 °C] buffer containing 20 mM NaCl and 0.1 mM EDTA. The proteins were fractionated employing three 5 mL HiTrap Q HP columns connected in tandem and developed with a 30-column volume linear gradient to 1 M NaCl. Fractions containing gpD were pooled, exchanged into 50 mM NaOAc [pH 4.8] buffer using Amicon centrifugal filter units (3k MWCO), and loaded onto three 5 mL HiTrap SP columns connected in tandem. Bound proteins were eluted with a 30-column volume linear gradient to 0.5 M NaCl, and gpD-containing fractions were pooled and dialyzed overnight against 20 mM Tris [pH 8.0, 4 °C] buffer containing 20 mM NaCl and 0.1 mM EDTA for storage at 4 °C. Alternatively, 20% glycerol was added to the samples for long-term storage at -80 °C.

Construction of D-F5M. Purified gpD(S42C) was exchanged into 0.01 M PBS [pH 6.6] buffer using Amicon centrifugal filter units (3k MWCO). Disulfide bonds were reduced with the addition of a 3-fold molar excess of Tris (2-carboxyethyl) phosphine (1 h, 25 °C). A 2-fold molar excess of F5M was then added, and the mixture incubated (1 h, 25 °C) to couple the sole cysteine residue in the protein. The reaction was quenched with the addition of 0.1% β-ME (30 min, 25 °C), and the modified protein exchanged into 40 mM Tris [pH 8.0, 4 °C] buffer containing 20 mM NaCl and 0.1 mM EDTA. Further polishing of D-F5M was done using Zeba spin desalting columns (7k MWCO) developed with the same buffer. Collections were pooled and stored at 4 °C. Protein concentration was quantified spectroscopically by comparing absorptions at 280 and 495 nm to a standard curve of unmodified F5M.

Construction of D-Trz. Trastuzumab was exchanged into 0.01 M PBS [pH 7.2] buffer using Amicon centrifugal filter units (100k MWCO). A 5-fold molar excess of Mal-PEG-VA was added, and the mixture incubated (30 min, 25 °C) to modify the accessible ε -amino groups of lysine residues. A 3-fold molar excess of reduced gpD(S42C) was added, and the mixture was incubated (1 h, 25 °C) to conjugate both proteins. The reaction was quenched with the

addition of 0.1% β -ME (30 min, 25 °C), and D-Trz exchanged into 40 mM Tris [pH 8.0, 4 °C] buffer containing 20 mM NaCl and 0.1 mM EDTA for storage at 4 °C. Protein concentration was quantified spectroscopically and by densitometry.

PLP Expansion and Decoration. Expanded PLPs were prepared and decorated in vitro with gpD proteins, as previously described³⁵ with modification. Briefly, purified PLPs were expanded with 2.5 M urea (30 min, on ice) and exchanged into 10 mM HEPES [pH 7.4] buffer containing 0.2 M urea using Amicon centrifugal filter units (100k MWCO). Expanded shells (30 nM) were decorated in a stepwise fashion with modified and wild-type gpD at 25 °C in 10 mM HEPES [pH 7.4] buffer containing 10 mM arginine, 0.05 M urea, and 0.1% Tween 20. Proteins were added in the following order: (1) D-F5M (3.47 µM final concentration, 20 min incubation); (2) D-Trz (0.07-4.16 µM final concentration, 20 min incubation); (3) wildtype gpD (6.24–10.32 μ M final concentration, 60 min incubation). Decorated PLPs were purified by SEC using a Superose 6 Increase column developed with 40 mM HEPES [pH 7.4] buffer containing 150 mM NaCl, 0.2 M arginine, 0.1 mM EDTA, and 2 mM β -ME at a flow rate of 0.3 mL/min. Fractions containing decorated PLPs were pooled and exchanged into 50 mM HEPES [pH 7.4] buffer containing 100 mM NaCl and 10 mM MgCl₂ for storage at 4 °C.

Transmission Electron Microscopy. Carbon-coated copper grids (300 mesh) were glow-discharged using a Pelco easiGlow glow discharge cleaning system (Ted Pella, Inc.; Redding, CA, USA) with a plasma current of 15 mA, negative glow discharge head polarity, and glow discharge duration of 1 min and held under vacuum for 15 s. PLP preparations were diluted to 20 nM using doubledistilled water and spotted onto grids. Following sample adsorption (15 s), excess liquid was wicked off using a Whatman #1 filter paper. Grids were washed using double-distilled water, and excess liquid was wicked off. Samples were negatively stained (15-20 s) with filtered 2% (w/v) methylamine tungstate [pH 6.7] and 50 μ g/mL bacitracin (0.2 µm Nucleopore polycarbonate syringe filters). Excess stain was wicked off, and grids were allowed to air-dry (≥1 h). Samples were maintained covered throughout this procedure and stored in a grid storage box at room temperature until imaged. Images were acquired on a FEI Tecnai G2 transmission electron microscope at an accelerating voltage of 80 kV and equipped with a 2k × 2k CCD camera. Images were processed in Fiji, 90 and measurements based on

Dynamic and Electrophoretic Light Scattering Measurements. Decorated particles were diluted to 50 μ L at 5 nM or 700 μ L at 10–15 nM using double-distilled water for dynamic light scattering and electrophoretic light scattering analyses, respectively. Particle size (Z-average [nm], intensity size distribution [nm], polydispersity [a.u.]) and overall surface charge (zeta potential [mV]) were measured using a Malvern Panalytical Zetasizer Nano ZS (He–Ne laser 633 nm light source; 5 mW maximum power) with a method specified for protein in water solution. Successive sample measurements were done in triplicate with calculated values reported as mean \pm standard deviation.

Cell Culture. Breast cancer cell lines (SKBR3, MDA-MB-231) were purchased from the Barbara Davis Center BioResources Core Facility Molecular Biology Unit, authenticated by short tandem repeat profiling, and tested for mycoplasma contamination. Cell lines were maintained at 37 °C, 5% CO₂ in McCoy's 5A media containing 1.5 mM $_{\rm L}$ -glutamine, 26.2 mM NaCO₃, and 16.7 mM glucose or Leibovitz's L-15 media containing 2.1 mM $_{\rm L}$ -glutamine and 5.0 mM galactose and supplemented with 26.2 mM NaCO₃, respectively. Both media were supplemented with 10% heat-inactivated fetal bovine serum (FBS), 10 mM HEPES, 1× MEM nonessential amino acids solution, 50 units/mL penicillin, and 50 μg/mL streptomycin and filtered using 0.2 μm Corning vacuum filters.

In Vitro PLP Internalization Assay. SKBR3 and MDA-MB-231 cells were seeded at densities of 1×10^4 cells/well or 2×10^4 cells/chamber for 96-well plates or Nunc Lab-Tek eight-chambered glass slides, respectively, and maintained in complete media (prepared as above) until \geq 60% confluency was achieved. Cells were then washed with PBS [pH 7.4] and treated with PLPs (2 nM) in complete media

at a final concentration of 20% FBS (3 h, 37 °C). Subsequent steps were performed at ambient temperature and included intermittent washes with PBS [pH 7.4]. Cells were fixed with 4% paraformaldehyde (PFA) and permeabilized with PBS [pH 7.4] containing 0.1% Triton X-100 and 1% bovine serum albumin (BSA). Immunocytochemical staining was performed using Alexa Fluor 594 AffiniPure goat anti-human IgG for detection of both native and modified Trz, and cell nuclei were stained using Hoechst 33342. Particle—cell interactions were imaged by fluorescence microscopy using a Nikon Eclipse Ts2 inverted confocal microscope equipped with a CF160 optical system. Fiji⁹⁰ was used for image processing.

Cytotoxicity Assay. SKBR3 and MDA-MB-231 cells were seeded at densities of 8.1×10^4 cells/well and cultured in complete media for 2 days. Cells were then washed with PBS [pH 7.4] and treated (3 h, 37 °C) with PLPs (2 nM) or Trz (150 nM or 2 μ M) in sextuplicate. DMSO (10%) was used as a positive control of toxicity, whereas PLP storage buffer diluted in PBS [pH 7.4] served as the vehicle control. The CytoTox-Glo cytotoxicity assay (Promega; Madison, WI, USA) was used to determine cell cytotoxicity, according to manufacturer specifications. Luminescence was measured using a SpectraMax M5 reader at an integration time of 1000 ms. The reported value was the calculated cell viability percentage normalized to mock treated cells with standard error of the mean (SEM) as error bars.

MTT Viability Assay. SKBR3 and MDA-MB-231 cells were seeded at densities of 4.4×10^4 cells/well and cultured in complete media for 2 days. Cells were then washed with PBS [pH 7.4] and treated (3 h, 37 °C) with PLPs (2 nM) or Trz (150 nM or 2 μ M) in sextuplicate. PLP storage buffer diluted in PBS [pH 7.4] served as the vehicle control. The Vybrant MTT cell proliferation assay (Molecular Probes, Inc., Eugene, OR, USA) was used to determine cell viability, according to manufacturer specifications. Incubations (4 h, 37 °C) with the MTT stock solution (12 mM) were performed in RPMI-1640 media minus phenol red and supplemented as described for complete media formulations. MTT stock solution diluted in media served as a negative control. Signal was developed using DMSO (10 min, 37 °C), and absorbance read at 540 nm using a SpectraMax M5 reader. Values reported as mean \pm SEM are based on the calculated metabolic activity percentage normalized to mock-treated cells.

Crystal Violet Proliferation and Viability Assay. SKBR3 cells were plated in duplicate at 2.5×10^5 cells/well in six-well plates, maintained and treated as described above. Cells were harvested by trypsinization, replated in triplicate at 5.0×10^4 cells/well in 24-well plates, and cultured in complete media. At the end of days 1, 3, 6, and 9, cells were fixed with 4% PFA and stained with crystal violet to stain proteins and DNA of viable, adherent cells. Optical density at 570 nm $({\rm OD}_{570})$ was measured, and the percentage of viable, treated cells calculated by comparing average ${\rm OD}_{570}$ values of treated cells to those of mock-treated cells. A minimum of three independent experimental replicates were performed.

Immunoblotting. For Western blot analysis, cells were washed twice in ice-cold PBS and lysed in 50 mM Tris-HCl [pH 7.4, 4 °C] buffer containing 150 mM NaCl, 1% NP-40, 0.5% sodium deoxycholate, 0.1% SDS and supplemented with a protease and phosphatase inhibitor cocktail. Protein concentration was determined spectroscopically, and 250 μ g of protein was loaded on SDS-PAGE gels for immunoblotting. Antibody stocks were diluted (1:2000) for the following: pan AKT, pAKT (Ser473), mTOR, pmTOR (Ser2448), HER2, pHER2 (Tyr1221/1222), β-actin, and rabbit anti-human IgG conjugated with horseradish peroxidase. A chemiluminescence system was used for detection, and representative blots were selected from a minimum of three independent experimental replicates.

UHPLC-MS Metabolomics. Metabolites were extracted from SKBR3 cell pellets ($\sim 1.0 \times 10^7$ cells) or supernatants (10 μL) in icecold buffer containing methanol, acetonitrile, and water (5:3:2, v/v/v) at a 1:10 or 1:25 dilution, respectively. Samples were vortexed, and insoluble material was pelleted. Supernatants were analyzed *via* UHPLC-MS (Vanquish–Q Exactive; Thermo Fisher Scientific; San Jose, CA, USA, and Bremen, Germany). Metabolites were resolved on a Kinetex XB C18 RP column (2.1 × 150 mm, 1.7 μm;

Phenomenex) at 45 °C using a 5 min gradient method. Technical mixes were generated by pooling aliquots of extracts and ran every 3 analytical runs to control for technical variability, as judged by coefficients of variation. Metabolite assignments and isotopologue distributions were performed using MAVEN⁹² (Princeton, NJ, USA).

Nano-UHPLC-Tandem MS Proteomics. Proteins extracted from cell pellets after metabolomic analysis were solubilized in 8 M urea and digested via filter-aided sample preparation (FASP). Extracted peptides were analyzed by nanoLC-MS/MS (Thermo EASY-nLC 1200-Orbitrap Fusion Lumos) and separated on a C18 analytical column (1.5 × 100 mm; house-made) packed with Cortecs C18 resin (2.7 mm; Phenomenex; Torrance, CA, USA), using a 180 min linear gradient of 6-38% acetonitrile (ACN) at 400 nL/min). Data acquisition was performed using the instrument supplied Xcalibur software (v4.1; Thermo Fisher Scientific), and raw files were converted to peak lists using Proteome Discoverer 2.1.0.62. Samples were analyzed using Mascot 2.6.1 (Matrix Science; London, ÛK) against the human UniProt database with specified variable modifications. Scaffold 4.9.0 (Proteome Software Inc., Portland, OR, USA) was used to validate MS/MS-based peptide and protein identifications.

Statistical Analysis. Statistical and multivariate analyses (*e.g., t* test, one-way repeated measures ANOVA, Dunnett's test, partial least-squares-discriminant analysis (PLS-DA), hierarchical clustering analysis (HCA)), heat maps, and graphs were performed and prepared using MetaboAnalyst 4.0, ⁹³ GraphPad Prism 5.0 (GraphPad Software, Inc., La Jolla, CA, USA), and Morpheus (Broad Institute, Boston, MA, USA). Statistical analysis shown in plots was performed by one-way repeated measures ANOVA, followed by Dunnett's multiple comparison test. The treatment group used as the control group in the Dunnett test is denoted by a black or red asterisk for mock or Trz-treated cells, respectively.

ASSOCIATED CONTENT

Supporting Information

The Supporting Information is available free of charge at https://pubs.acs.org/doi/10.1021/acsnano.1c02864.

Supplemental figures and table to include data corresponding to the characterization of lambda PLPs; the characterization of conjugation and lambda PLP decoration reactions; control studies for the lambda PLP internalization assay; quantitation of Trz-PLP internalization by HER2⁺ cells; the biological assessment of HER2⁺ cells treated with Trz-PLPs; lambda PLP toxicity and effects on metabolic activity; the impact of HER2-targeted treatment on the metabolome of HER2⁺ cells; the treatment effects on amino acid metabolism and cell proliferation for HER2⁺ cells (PDF)

Table S2: Proteomics report (raw data, statistics, etc.) for analyses on HER2⁺ cells (XLSX)

Table S3: Metabolomics report (raw data, statistics, etc.) for analyses on HER2⁺ cells and media extracts (XLSX)

AUTHOR INFORMATION

Corresponding Author

Carlos E. Catalano — Department of Pharmaceutical Sciences, Skaggs School of Pharmacy and Pharmaceutical Sciences and Program in Structural Biology and Biochemistry, University of Colorado Anschutz Medical Campus, Aurora, Colorado 80045, United States; orcid.org/0000-0003-2349-5758; Phone: +1 (303) 724-0011; Email: carlos.catalano@cuanschutz.edu

Authors

Alexis Catala – Department of Biochemistry and Molecular Genetics, School of Medicine and Program in Structural Biology and Biochemistry, University of Colorado Anschutz Medical Campus, Aurora, Colorado 80045, United States

Monika Dzieciatkowska – Department of Biochemistry and Molecular Genetics, School of Medicine, University of Colorado Anschutz Medical Campus, Aurora, Colorado 80045, United States

Guankui Wang – Department of Pharmaceutical Sciences, Skaggs School of Pharmacy and Pharmaceutical Sciences, University of Colorado Anschutz Medical Campus, Aurora, Colorado 80045, United States

Arthur Gutierrez-Hartmann — Departments of Biochemistry and Molecular Genetics and Medicine — Division of Endocrinology, School of Medicine, University of Colorado Anschutz Medical Campus, Aurora, Colorado 80045, United States

Dmitri Simberg – Department of Pharmaceutical Sciences, Skaggs School of Pharmacy and Pharmaceutical Sciences, University of Colorado Anschutz Medical Campus, Aurora, Colorado 80045, United States

Kirk C. Hansen – Department of Biochemistry and Molecular Genetics, School of Medicine and Program in Structural Biology and Biochemistry, University of Colorado Anschutz Medical Campus, Aurora, Colorado 80045, United States

Angelo D'Alessandro – Departments of Biochemistry and Molecular Genetics and Medicine – Division of Hematology, School of Medicine and Program in Structural Biology and Biochemistry, University of Colorado Anschutz Medical Campus, Aurora, Colorado 80045, United States

Complete contact information is available at: https://pubs.acs.org/10.1021/acsnano.1c02864

Author Contributions

G.W. and D.S. generously provided the trastuzumab and Mal-PEG-SVA used in these studies. A.C. performed all of the studies with the exception of the proteomics, which was done by M.D. A.C. performed the data analysis. Contributions to data interpretation were provided by A.G.H. and C.E.C. (proliferation, immunoblotting studies); A.D.A. (metabolomics); A.D.A. and K.C.H. (proteomics). Study design, figures, and initial draft of the manuscript were done by A.C. and C.E.C. All coauthors contributed to preparing the final manuscript.

Funding

The research reported herein was supported by the NSF #MCB1158107 (C.E.C.) and #GRFP1553798 (A.C.), the University of Colorado School of Pharmacy Associate Dean of Research Seed Grant program (C.E.C., A.G.H.), and the NIH National Institute of General and Medical Sciences #RM1GM131968 (A.D.A., K.C.H.) and National Heart, Lung and Blood Institute #R21HL150032 (A.D.A.). Any opinions, findings, conclusions, or recommendations expressed are those of the authors and do not necessarily reflect the views of the NSF or NIH.

Notes

The authors declare no competing financial interest; however, the authors disclose that A.D.A. is a founder of Omix Technologies, Inc. and Altis Biosciences, LLC. and a consultant for Hemanext, Inc. and New Health Sciences, Inc. Additionally, A.D.A. and K.C.H. are founders of Endura, LLC.

ACKNOWLEDGMENTS

The authors would like to thank T. Trudeau for assistance in the development of the proliferation assay and immunoblotting studies, U. Kompella for use of the SpectraMax M5 reader and Malvern Zetasizer, J. Bourne for her assistance in the Electron Microscopy Center, and D. Siegel for training on the Skaggs School of Pharmacy confocal microscope. The original structural data for the lambda capsid depicted in Figure ¹,A were kindly provided by G. Lander.

REFERENCES

- (1) Knipe, D. M.; Howley, P. M.; Fields, B. N. Virology, 5th ed.; Wolters Kluwer Health/Lippincott Williams & Wilkins: New York, NY: 2007.
- (2) Calendar, R.; Abedon, S. T.; Calendar, R. The Bacteriophages, 2nd ed.; Oxford University Press, Inc.: New York, NY: 2006; p 746.
- (3) Fokine, A.; Rossmann, M. G. Molecular Architecture of Tailed Double-Stranded DNA Phages. *Bacteriophage* **2014**, *4* (1), e28281.
- (4) Beghetto, E.; Gargano, N. Lambda-Display: A Powerful Tool for Antigen Discovery. *Molecules* **2011**, *16* (4), 3089–105.
- (5) Schwarz, B.; Madden, P.; Avera, J.; Gordon, B.; Larson, K.; Miettinen, H. M.; Uchida, M.; LaFrance, B.; Basu, G.; Rynda-Apple, A.; Douglas, T. Symmetry Controlled, Genetic Presentation of Bioactive Proteins on the P22 Virus-Like Particle Using an External Decoration Protein. ACS Nano 2015, 9 (9), 9134–47.
- (6) Steinmetz, N. F. Biological and Evolutionary Concepts for Nanoscale Engineering: Viruses as Natural Nanoparticles Have Great Potential for a Wide Range of Nanoscale Products. *EMBO Rep.* **2019**, 20 (8), e48806.
- (7) Karimi, M.; Mirshekari, H.; Moosavi Basri, S. M.; Bahrami, S.; Moghoofei, M.; Hamblin, M. R. Bacteriophages and Phage-Inspired Nanocarriers for Targeted Delivery of Therapeutic Cargos. *Adv. Drug Delivery Rev.* **2016**, *106*, 45–62.
- (8) Koudelka, K. J.; Pitek, A. S.; Manchester, M.; Steinmetz, N. F. Virus-Based Nanoparticles as Versatile Nanomachines. *Annu. Rev. Virol.* **2015**, *2* (1), 379–401.
- (9) Clark, J. R.; March, J. B. Bacteriophages and Biotechnology: Vaccines, Gene Therapy and Antibacterials. *Trends Biotechnol.* **2006**, 24 (5), 212–8.
- (10) Tao, P.; Zhu, J.; Mahalingam, M.; Batra, H.; Rao, V. B. Bacteriophage T4 Nanoparticles for Vaccine Delivery Against Infectious Diseases. *Adv. Drug Delivery Rev.* **2019**, *145*, 57–72.
- (11) Czapar, A. E.; Steinmetz, N. F. Plant Viruses and Bacteriophages for Drug Delivery in Medicine and Biotechnology. *Curr. Opin. Chem. Biol.* **2017**, *38*, 108–116.
- (12) Tao, P.; Mahalingam, M.; Marasa, B. S.; Zhang, Z.; Chopra, A. K.; Rao, V. B. *In Vitro* and *in Vivo* Delivery of Genes and Proteins Using the Bacteriophage T4 DNA Packaging Machine. *Proc. Natl. Acad. Sci. U. S. A.* 2013, 110 (15), 5846–51.
- (13) Chhibber, S.; Kaur, S.; Kumari, S. Therapeutic Potential of Bacteriophage in Treating Klebsiella Pneumoniae B5055-Mediated Lobar Pneumonia in Mice. J. Med. Microbiol. 2008, 57, 1508–1513.
- (14) Bruttin, A.; Brussow, H. Human Volunteers Receiving Escherichia Coli Phage T4 Orally: A Safety Test of Phage Therapy. *Antimicrob. Agents Chemother.* **2005**, *49* (7), 2874–8.
- (15) Rhoads, D. D.; Wolcott, R. D.; Kuskowski, M. A.; Wolcott, B. M.; Ward, L. S.; Sulakvelidze, A. Bacteriophage Therapy of Venous Leg Ulcers in Humans: Results of a Phase I Safety Trial. *J. Wound Care* **2009**, *18* (6), 237–8. 240–3.
- (16) Yildiz, I.; Shukla, S.; Steinmetz, N. F. Applications of Viral Nanoparticles in Medicine. *Curr. Opin. Biotechnol.* **2011**, 22 (6), 901–8.
- (17) Campbell, A. M. Bacteriophage Lambda as a Model System. *BioEssays* **1986**, 5 (6), 277–80.
- (18) Roach, D. R.; Debarbieux, L. Phage Therapy: Awakening a Sleeping Giant. *Emerg Top Life Sci.* **2017**, *1* (1), 93–103.

- (19) Koudelka, K. J.; Ippoliti, S.; Medina, E.; Shriver, L. P.; Trauger, S. A.; Catalano, C. E.; Manchester, M. Lysine Addressability and Mammalian Cell Interactions of Bacteriophage Lambda Procapsids. *Biomacromolecules* **2013**, *14* (12), 4169–76.
- (20) Chang, J. R.; Song, E. H.; Nakatani-Webster, E.; Monkkonen, L.; Ratner, D. M.; Catalano, C. E. Phage Lambda Capsids as Tunable Display Nanoparticles. *Biomacromolecules* **2014**, *15* (12), 4410–9.
- (21) Iwagami, Y.; Casulli, S.; Nagaoka, K.; Kim, M.; Carlson, R. I.; Ogawa, K.; Lebowitz, M. S.; Fuller, S.; Biswas, B.; Stewart, S.; Dong, X.; Ghanbari, H.; Wands, J. R. Lambda Phage-Based Vaccine Induces Antitumor Immunity in Hepatocellular Carcinoma. *Heliyon* **2017**, 3 (9), e00407.
- (22) Arab, A.; Nicastro, J.; Slavcev, R.; Razazan, A.; Barati, N.; Nikpoor, A. R.; Brojeni, A. A. M.; Mosaffa, F.; Badiee, A.; Jaafari, M. R.; Behravan, J. Lambda Phage Nanoparticles Displaying HER2-Derived E75 Peptide Induce Effective E75-CD8(+) T Response. *Immunol. Res.* **2018**, *66* (1), 200–206.
- (23) Razazan, A.; Nicastro, J.; Slavcev, R.; Barati, N.; Arab, A.; Mosaffa, F.; Jaafari, M. R.; Behravan, J. Lambda Bacteriophage Nanoparticles Displaying GP2, a HER2/neu Derived Peptide, Induce Prophylactic and Therapeutic Activities against Tubo Tumor Model in Mice. Sci. Rep. 2019, 9 (1), 2221.
- (24) Brune, K. D.; Leneghan, D. B.; Brian, I. J.; Ishizuka, A. S.; Bachmann, M. F.; Draper, S. J.; Biswas, S.; Howarth, M. Plug-And-Display: Decoration of Virus-Like Particles *via* Isopeptide Bonds for Modular Immunization. *Sci. Rep.* **2016**, *6*, 19234.
- (25) Stephanopoulos, N.; Tong, G. J.; Hsiao, S. C.; Francis, M. B. Dual-Surface Modified Virus Capsids for Targeted Delivery of Photodynamic Agents to Cancer Cells. *ACS Nano* **2010**, *4* (10), 6014–20.
- (26) Carrico, Z. M.; Farkas, M. E.; Zhou, Y.; Hsiao, S. C.; Marks, J. D.; Chokhawala, H.; Clark, D. S.; Francis, M. B. N-Terminal Labeling of Filamentous Phage to Create Cancer Marker Imaging Agents. *ACS Nano* **2012**, *6* (8), 6675–80.
- (27) Patterson, D. P.; Prevelige, P. E.; Douglas, T. Nanoreactors by Programmed Enzyme Encapsulation Inside the Capsid of the Bacteriophage P22. ACS Nano 2012, 6 (6), 5000–9.
- (28) Fiedler, J. D.; Fishman, M. R.; Brown, S. D.; Lau, J.; Finn, M. G. Multifunctional Enzyme Packaging and Catalysis in the Qbeta Protein Nanoparticle. *Biomacromolecules* **2018**, *19* (10), 3945–3957.
- (29) Lucon, J.; Qazi, S.; Uchida, M.; Bedwell, G. J.; LaFrance, B.; Prevelige, P. E., Jr.; Douglas, T. Use of the Interior Cavity of the P22 Capsid for Site-Specific Initiation of Atom-Transfer Radical Polymerization with High-Density Cargo Loading. *Nat. Chem.* **2012**, *4* (10), 781–8.
- (30) Uchida, M.; Morris, D. S.; Kang, S.; Jolley, C. C.; Lucon, J.; Liepold, L. O.; LaFrance, B.; Prevelige, P. E., Jr.; Douglas, T. Site-Directed Coordination Chemistry with P22 Virus-Like Particles. *Langmuir* **2012**, 28 (4), 1998–2006.
- (31) Fang, P. Y.; Gomez Ramos, L. M.; Holguin, S. Y.; Hsiao, C.; Bowman, J. C.; Yang, H. W.; Williams, L. D. Functional RNAs: Combined Assembly and Packaging in VLPs. *Nucleic Acids Res.* **2017**, 45 (6), 3519–3527.
- (32) Lee, T. J.; Haque, F.; Shu, D.; Yoo, J. Y.; Li, H.; Yokel, R. A.; Horbinski, C.; Kim, T. H.; Kim, S. H.; Kwon, C. H.; Nakano, I.; Kaur, B.; Guo, P.; Croce, C. M. RNA Nanoparticle as a Vector for Targeted siRNA Delivery into Glioblastoma Mouse Model. *Oncotarget* **2015**, *6* (17), 14766–76.
- (33) Catalano, C. E. Bacteriophage Lambda: The Path from Biology to Theranostic Agent. Wiley Interdiscip. Rev.: Nanomed. Nanobiotechnol. 2018, 10 (5), e1517.
- (34) Medina, E. M.; Andrews, B. T.; Nakatani, E.; Catalano, C. E. The Bacteriophage Lambda gpNu3 Scaffolding Protein Is an Intrinsically Disordered and Biologically Functional Procapsid Assembly Catalyst. *J. Mol. Biol.* **2011**, *412* (4), 723–36.
- (35) Medina, E.; Nakatani, E.; Kruse, S.; Catalano, C. E. Thermodynamic Characterization of Viral Procapsid Expansion into a Functional Capsid Shell. *J. Mol. Biol.* **2012**, *418* (3–4), 167–80.

- (36) Lander, G. C.; Evilevitch, A.; Jeembaeva, M.; Potter, C. S.; Carragher, B.; Johnson, J. E. Bacteriophage Lambda Stabilization by Auxiliary Protein gpD: Timing, Location, and Mechanism of Attachment Determined by Cryo-Em. *Structure* **2008**, *16* (9), 1399–406.
- (37) Singh, P.; Nakatani, E.; Goodlett, D. R.; Catalano, C. E. A Pseudo-Atomic Model for the Capsid Shell of Bacteriophage Lambda Using Chemical Cross-Linking/Mass Spectrometry and Molecular Modeling. *J. Mol. Biol.* **2013**, 425 (18), 3378–88.
- (38) Nicastro, J.; Sheldon, K.; Slavcev, R. A. Bacteriophage Lambda Display Systems: Developments and Applications. *Appl. Microbiol. Biotechnol.* **2014**, 98 (7), 2853–66.
- (39) Robertson, T. A.; Bunel, F.; Roberts, M. S. Fluorescein Derivatives in Intravital Fluorescence Imaging. *Cells* **2013**, 2 (3), 591–606
- (40) Goldenberg, M. M. Trastuzumab, a Recombinant DNA-Derived Humanized Monoclonal Antibody, a Novel Agent for the Treatment of Metastatic Breast Cancer. *Clin. Ther.* **1999**, *21* (2), 309–18
- (41) Bertelsen, V.; Stang, E. The Mysterious Ways of ErbB2/HER2 Trafficking. *Membranes (Basel, Switz.)* **2014**, *4* (3), 424–46.
- (42) Iqbal, N.; Iqbal, N. Human Epidermal Growth Factor Receptor 2 (HER2) in Cancers: Overexpression and Therapeutic Implications. *Mol. Biol. Int.* **2014**, 2014, 852748.
- (43) Larionov, A. A. Current Therapies for Human Epidermal Growth Factor Receptor 2-Positive Metastatic Breast Cancer Patients. *Front. Oncol.* **2018**, *8*, 89.
- (44) Slamon, D. J.; Leyland-Jones, B.; Shak, S.; Fuchs, H.; Paton, V.; Bajamonde, A.; Fleming, T.; Eiermann, W.; Wolter, J.; Pegram, M.; Baselga, J.; Norton, L. Use of Chemotherapy plus a Monoclonal Antibody against HER2 for Metastatic Breast Cancer That Overexpresses HER2. N. Engl. J. Med. 2001, 344 (11), 783–92.
- (45) Baselga, J.; Norton, L.; Albanell, J.; Kim, Y. M.; Mendelsohn, J. Recombinant Humanized Anti-HER2 Antibody (Herceptin) Enhances the Antitumor Activity of Paclitaxel and Doxorubicin against HER2/neu Overexpressing Human Breast Cancer Xenografts. *Cancer Res.* 1998, 58 (13), 2825–2831.
- (46) Sawyers, C. L. Herceptin: A First Assault on Oncogenes That Launched a Revolution. *Cell* **2019**, *179* (1), 8–12.
- (47) Ayoub, N. M.; Al-Shami, K. M.; Yaghan, R. J. Immunotherapy for HER2-Positive Breast Cancer: Recent Advances and Combination Therapeutic Approaches. *Breast Cancer: Targets Ther.* **2019**, *11*, 53–60
- (48) Perez-Herrero, E.; Fernandez-Medarde, A. Advanced Targeted Therapies in Cancer: Drug Nanocarriers, the Future of Chemotherapy. *Eur. J. Pharm. Biopharm.* **2015**, *93*, 52–79.
- (49) Kumler, I.; Tuxen, M. K.; Nielsen, D. L. A Systematic Review of Dual Targeting in HER2-Positive Breast Cancer. *Cancer Treat. Rev.* **2014**, *40* (2), 259–70.
- (50) Chen, Y.; Batra, H.; Dong, J.; Chen, C.; Rao, V. B.; Tao, P. Genetic Engineering of Bacteriophages against Infectious Diseases. *Front. Microbiol.* **2019**, *10*, 954.
- (51) Wen, A. M.; Shukla, S.; Saxena, P.; Aljabali, A. A.; Yildiz, I.; Dey, S.; Mealy, J. E.; Yang, A. C.; Evans, D. J.; Lomonossoff, G. P.; Steinmetz, N. F. Interior Engineering of a Viral Nanoparticle and Its Tumor Homing Properties. *Biomacromolecules* **2012**, *13* (12), 3990–4001.
- (52) Lazar, A. C.; Wang, L.; Blattler, W. A.; Amphlett, G.; Lambert, J. M.; Zhang, W. Analysis of the Composition of Immunoconjugates Using Size-Exclusion Chromatography Coupled to Mass Spectrometry. *Rapid Commun. Mass Spectrom.* **2005**, *19* (13), 1806–14.
- (53) Tsuchikama, K.; An, Z. Antibody-Drug Conjugates: Recent Advances in Conjugation and Linker Chemistries. *Protein Cell* **2018**, 9 (1), 33–46.
- (54) Lofblom, J.; Feldwisch, J.; Tolmachev, V.; Carlsson, J.; Stahl, S.; Frejd, F. Y. Affibody Molecules: Engineered Proteins for Therapeutic, Diagnostic and Biotechnological Applications. *FEBS Lett.* **2010**, *584* (12), 2670–80.

- (55) Garg, P.; Ceccarelli, D. F.; Keszei, A. F. A.; Kurinov, I.; Sicheri, F.; Sidhu, S. S. Structural and Functional Analysis of Ubiquitin-Based Inhibitors That Target the Backsides of E2 Enzymes. *J. Mol. Biol.* **2020**, 432 (4), 952–966.
- (56) Satpathy, M.; Wang, L.; Zielinski, R. J.; Qian, W.; Wang, Y. A.; Mohs, A. M.; Kairdolf, B. A.; Ji, X.; Capala, J.; Lipowska, M.; Nie, S.; Mao, H.; Yang, L. Targeted Drug Delivery and Image-Guided Therapy of Heterogeneous Ovarian Cancer Using HER2-Targeted Theranostic Nanoparticles. *Theranostics* **2019**, *9* (3), 778–795.
- (57) Abdifetah, O.; Na-Bangchang, K. Pharmacokinetic Studies of Nanoparticles as a Delivery System for Conventional Drugs and Herb-Derived Compounds for Cancer Therapy: A Systematic Review. *Int. J. Nanomed.* **2019**, *14*, 5659–5677.
- (58) Maculins, T.; Garcia-Pardo, J.; Skenderovic, A.; Gebel, J.; Putyrski, M.; Vorobyov, A.; Busse, P.; Varga, G.; Kuzikov, M.; Zaliani, A.; Rahighi, S.; Schaeffer, V.; Parnham, M. J.; Sidhu, S. S.; Ernst, A.; Dotsch, V.; Akutsu, M.; Dikic, I. Discovery of Protein-Protein Interaction Inhibitors by Integrating Protein Engineering and Chemical Screening Platforms. *Cell. Chem. Biol.* **2020**, *27* (11), 1441–1451.
- (59) Herceg, V.; Bouilloux, J.; Janikowska, K.; Allemann, E.; Lange, N. Cathepsin B-Cleavable Cyclopeptidic Chemotherapeutic Prodrugs. *Molecules* **2020**, 25 (18), 4285.
- (60) Johnston, S. T.; Faria, M.; Crampin, E. J. An Analytical Approach for Quantifying the Influence of Nanoparticle Polydispersity on Cellular Delivered Dose. *J. R. Soc., Interface* **2018**, *15* (144), 20180364.
- (61) Frohlich, E. The Role of Surface Charge in Cellular Uptake and Cytotoxicity of Medical Nanoparticles. *Int. J. Nanomed.* **2012**, *7*, 5577–91
- (62) Lakayan, D.; Haselberg, R.; Gahoual, R.; Somsen, G. W.; Kool, J. Affinity Profiling of Monoclonal Antibody and Antibody-Drug-Conjugate Preparations by Coupled Liquid Chromatography-Surface Plasmon Resonance Biosensing. *Anal. Bioanal. Chem.* **2018**, *410* (30), 7837–7848.
- (63) Niles, A. L.; Moravec, R. A.; Eric Hesselberth, P.; Scurria, M. A.; Daily, W. J.; Riss, T. L. A Homogeneous Assay to Measure Live and Dead Cells in the Same Sample by Detecting Different Protease Markers. *Anal. Biochem.* **2007**, 366 (2), 197–206.
- (64) Mosmann, T. Rapid Colorimetric Assay for Cellular Growth and Survival: Application to Proliferation and Cytotoxicity Assays. *J. Immunol. Methods* **1983**, *65* (1–2), 55–63.
- (65) Murray Stewart, T.; Dunston, T. T.; Woster, P. M.; Casero, R. A., Jr. Polyamine Catabolism and Oxidative Damage. *J. Biol. Chem.* **2018**, 293 (48), 18736–18745.
- (66) Zhang, Y.; Morar, M.; Ealick, S. E. Structural Biology of the Purine Biosynthetic Pathway. *Cell. Mol. Life Sci.* **2008**, *65* (23), 3699–724.
- (67) Nemkov, T.; Sun, K.; Reisz, J. A.; Song, A.; Yoshida, T.; Dunham, A.; Wither, M. J.; Francis, R. O.; Roach, R. C.; Dzieciatkowska, M.; Rogers, S. C.; Doctor, A.; Kriebardis, A.; Antonelou, M.; Papassideri, I.; Young, C. T.; Thomas, T. A.; Hansen, K. C.; Spitalnik, S. L.; Xia, Y.; Zimring, J. C.; Hod, E. A.; D'Alessandro, A. Hypoxia Modulates the Purine Salvage Pathway and Decreases Red Blood Cell and Supernatant Levels of Hypoxanthine during Refrigerated Storage. *Haematologica* 2018, 103 (2), 361–372.
- (68) Lieu, E. L.; Nguyen, T.; Rhyne, S.; Kim, J. Amino Acids in Cancer. Exp. Mol. Med. **2020**, 52 (1), 15–30.
- (69) Hendriks, B. S.; Wiley, H. S.; Lauffenburger, D. HER2-Mediated Effects on EGFR Endosomal Sorting: Analysis of Biophysical Mechanisms. *Biophys. J.* **2003**, 85 (4), 2732–45.
- (70) Zhu, W.; Okollie, B.; Artemov, D. Controlled Internalization of HER2/neu Receptors by Cross-Linking for Targeted Delivery. *Cancer Biol. Ther.* **2007**, *6* (12), 1960–6.
- (71) Friedman, L. M.; Rinon, A.; Schechter, B.; Lyass, L.; Lavi, S.; Bacus, S. S.; Sela, M.; Yarden, Y. Synergistic Down-Regulation of Receptor Tyrosine Kinases by Combinations of mAbs: Implications for Cancer Immunotherapy. *Proc. Natl. Acad. Sci. U. S. A.* **2005**, *102* (6), 1915–20.

- (72) Ben-Kasus, T.; Schechter, B.; Lavi, S.; Yarden, Y.; Sela, M. Persistent Elimination of ErbB/HER2-Overexpressing Tumors Using Combinations of Monoclonal Antibodies: Relevance of Receptor Endocytosis. *Proc. Natl. Acad. Sci. U. S. A.* 2009, 106 (9), 3294–9.
- (73) Tietjen, G. T.; Bracaglia, L. G.; Saltzman, W. M.; Pober, J. S. Focus on Fundamentals: Achieving Effective Nanoparticle Targeting. *Trends Mol. Med.* **2018**, 24 (7), 598–606.
- (74) Krishnamurti, U.; Silverman, J. F. HER2 in Breast Cancer: A Review and Update. Adv. Anat. Pathol. 2014, 21 (2), 100-7.
- (75) Arteaga, C. L.; Sliwkowski, M. X.; Osborne, C. K.; Perez, E. A.; Puglisi, F.; Gianni, L. Treatment of HER2-Positive Breast Cancer: Current Status and Future Perspectives. *Nat. Rev. Clin. Oncol.* **2012**, 9 (1), 16–32.
- (76) Kar, A.; Liu, B.; Gutierrez-Hartmann, A. ESE-1 Knockdown Attenuates Growth in Trastuzumab-Resistant HER2(+) Breast Cancer Cells. *Anticancer Res.* **2017**, 37 (12), 6583–6591.
- (77) Szymonowicz, K.; Oeck, S.; Malewicz, N. M.; Jendrossek, V. New Insights into Protein Kinase B/AKT Signaling: Role of Localized AKT Activation and Compartment-Specific Target Proteins for the Cellular Radiation Response. *Cancers* **2018**, *10* (3), 78.
- (78) Copp, J.; Manning, G.; Hunter, T. TORC-Specific Phosphorylation of Mammalian Target of Rapamycin (mTOR): Phospho-Ser2481 Is a Marker for Intact mTOR Signaling Complex 2. Cancer Res. 2009, 69 (5), 1821–7.
- (79) Muthuswamy, S. K.; Gilman, M.; Brugge, J. S. Controlled Dimerization of ErbB Receptors Provides Evidence for Differential Signaling by Homo- and Heterodimers. *Mol. Cell. Biol.* **1999**, *19* (10), 6845–57.
- (80) Dai, C.; Arceo, J.; Arnold, J.; Sreekumar, A.; Dovichi, N. J.; Li, J.; Littlepage, L. E. Metabolomics of Oncogene-Specific Metabolic Reprogramming during Breast Cancer. *Cancer Metab* **2018**, *6*, 5.
- (81) Lucantoni, F.; Dussmann, H.; Prehn, J. H. M. Metabolic Targeting of Breast Cancer Cells with the 2-Deoxy-D-Glucose and the Mitochondrial Bioenergetics Inhibitor MDIVI-1. *Front. Cell Dev. Biol.* **2018**, *6*, 113.
- (82) Gandhi, N.; Das, G. M. Metabolic Reprogramming in Breast Cancer and Its Therapeutic Implications. *Cells* **2019**, *8* (2), 89.
- (83) Huang, J.; Fraser, M. E. Structural Basis for the Binding of Succinate to Succinyl-CoA Synthetase. *Acta Crystallogr. D Struct Biol.* **2016**, 72, 912–21.
- (84) Xu, I. M.; Lai, R. K.; Lin, S. H.; Tse, A. P.; Chiu, D. K.; Koh, H. Y.; Law, C. T.; Wong, C. M.; Cai, Z.; Wong, C. C.; Ng, I. O. Transketolase Counteracts Oxidative Stress to Drive Cancer Development. *Proc. Natl. Acad. Sci. U. S. A.* **2016**, *113* (6), e725–34.
- (85) Yin, J.; Ren, W.; Huang, X.; Deng, J.; Li, T.; Yin, Y. Potential Mechanisms Connecting Purine Metabolism and Cancer Therapy. *Front. Immunol.* **2018**, *9*, 1697.
- (86) Xu, X.; Zur Hausen, A.; Coy, J. F.; Lochelt, M. TKTL1 Is Required for Rapid Cell Growth and Full Viability of Human Tumor Cells. *Int. J. Cancer* **2009**, 124 (6), 1330–7.
- (87) Manning, B. D.; Toker, A. AKT/Protein Kinase B Signaling: Navigating the Network. *Cell* **2017**, *169* (3), 381–405.
- (88) Lara, P. C.; Pruschy, M.; Zimmermann, M.; Henriquez-Hernandez, L. A. MVP and Vaults: A Role in the Radiation Response. *Radiat. Oncol.* **2011**, *6*, 148.
- (89) Yang, Q.; Catalano, C. E. Biochemical Characterization of Bacteriophage Lambda Genome Packaging *in Vitro. Virology* **2003**, 305 (2), 276–87.
- (90) Schindelin, J.; Arganda-Carreras, I.; Frise, E.; Kaynig, V.; Longair, M.; Pietzsch, T.; Preibisch, S.; Rueden, C.; Saalfeld, S.; Schmid, B.; Tinevez, J. Y.; White, D. J.; Hartenstein, V.; Eliceiri, K.; Tomancak, P.; Cardona, A. Fiji: An Open-Source Platform for Biological-Image Analysis. *Nat. Methods* **2012**, *9* (7), 676–82.
- (91) Catala, A.; Culp-Hill, R.; Nemkov, T.; D'Alessandro, A. Quantitative Metabolomics Comparison of Traditional Blood Draws and TAP Capillary Blood Collection. *Metabolomics* **2018**, *14* (7), 100. (92) Melamud, E.; Vastag, L.; Rabinowitz, J. D. Metabolomic
- (92) Melamud, E.; Vastag, L.; Rabinowitz, J. D. Metabolomic Analysis and Visualization Engine for LC-MS Data. *Anal. Chem.* **2010**, 82 (23), 9818–26.

(93) Chong, J.; Soufan, O.; Li, C.; Caraus, I.; Li, S.; Bourque, G.; Wishart, D. S.; Xia, J. Metaboanalyst 4.0: Towards More Transparent and Integrative Metabolomics Analysis. *Nucleic Acids Res.* **2018**, 46 (W1), W486–W494.